NASA CR-66882

PLANETARY ENVIRONMENT SIMULATION

Martian Sand And Dust Storm Simulation And Evaluation

By

G.L. Adlon, R.K. Weinberger, and D.R. McClure

Prepared under Contract No. NAS 1-8708

MCDONNELL DOUGLAS ASTRONAUTICS COMPANY
EASTERN DIVISION
ST. LOUIS, MISSOURI

for

NATIONAL AERONAUTICS AND SPACE ADMINISTRATION

TABLE OF CONTENTS

LIST OF FIGURES AND TABLES

NOMENCLATURE

A	Projected area of particle
A_2	Constant
a	Total particle acceleration
a_x	Horizontal particle acceleration
a_y	Vertical particle acceleration
B	Constant
C	Constant
c	Speed of sound for air
C_D	Coefficient of drag, $\frac{D}{1/2\ \rho_\infty U_R^2 A}$
D	Drag force on particle
d	Particle diameter
e	Logarithmic constant, 2.718
F_x	Horizontal forces on particle
F_y	Vertical forces on particle
g	Acceleration of gravity
Kn	Knudsen number, $1.28\sqrt{\gamma}\ M/Re_d$

L	Lift force on particle
l	Particle free path
M	Mach number, $\frac{U_R}{c}$
m	Particle mass
P_s	Chamber static pressure
$\frac{P(L/D)}{(L/D)}$	Probable error in L/D
$\frac{P(C_D)}{C_D}$	Probable error in C_D
R	Gas constant for air
r	Particle radius, d/2
Re_d	Reynolds number, $\frac{\rho_\infty d U_R}{\mu}$
T	Chamber static temperature
t	Time
U_∞	Gas flow velocity
U_p	Total particle velocity
U_R	Particle velocity relative to gas flow, $(U_\infty - U_p)$
U_x	Horizontal particle velocity
U_y	Vertical particle velocity

v	Particle velocity relative to gas flow, U_R
Δ_p	Dynamic pressure
γ	Ratio of specific heats
δ_L	Boundary sublayer thickness
δ_T	Blasius turbulent boundary layer thickness
μ	Microns; gas viscosity
π	Ratio of the circumference of a circle to its diameter, 3.14159265+
ρ_∞	Freestream gas density
ρ_p	Particle density

1. INTRODUCTION

Literature reviews disclosed that investigators have studied sand and dust transport mechanisms with particles either entrained in a medium[1,2,3] or at rest on a particle bed within the medium.[4,5] However, no literature could be found reporting studies of particle behavior in high-velocity, low-density gas streams such as might be found under postulated Martian environmental conditions. Although extrapolation of Earth-atmosphere sand/dust storm data has proved to be useful in predicting the gross behavior of such storms on Mars,[6,7] prediction of the behavior of individual particles, particularly during initiation of a storm, requires empirical data not found in literature.

Earlier work at McDonnell Douglas demonstrated that threshold velocities for the initiation of sand and dust storms could be measured under simulated Martian atmospheric pressure conditions.[8,9] However, no attempt was made then to observe individual particles or small groups of particles.

This report describes some of the basic phenomena observed during the study of single particle dynamics under postulated Martian surface wind conditions.

1.1 REVIEW OF SOLID-GAS FLOW. Many theories have been formalized explaining the mechanics of particle entrainment. The results of these studies differ appreciably from one another as may be seen in Figure 1.

Some investigators are satisfied with the concept of shearing stress being the only important parameter on which to base their analysis. Sir George Stokes established his law of motion of a sphere through a homogeneous medium

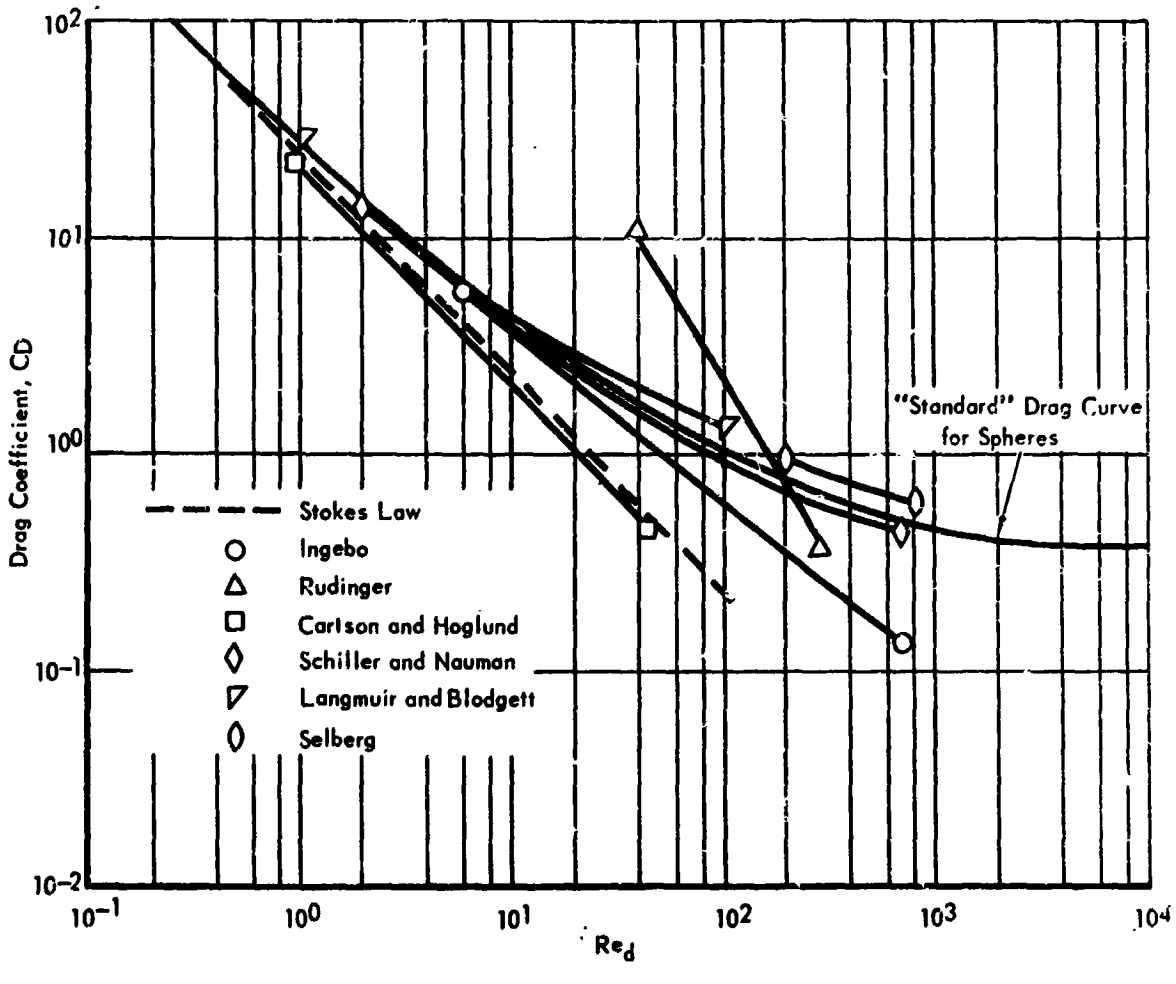

Figure 1 – Drag Coefficient for Spherical Bodies

$$F = 6\pi\mu r v$$

on this concept.

The possibility of lift forces acting on soil particles is seldom considered. However, early analytical studies by Jeffreys[10] and experimental studies by Chepil[11] tend to confirm the presence of these lift forces. Chepil contends that the composite lift force acting on a soil bed is actually 85 percent as great as the drag force and contributes substantially to soil transport.

Torobin and Gauvin[12-16] made a thorough literature survey on "The Fundamental Aspects of Solid-Gas Flow." They list and discuss the effects of particle rotation, roughness, and shape; the accelerated motion of a particle in a fluid; the sphere wake in a steady laminar flow; and fluid turbulence on the particle drag coefficient.

Schiller and Nauman[17] corrected the Stokesian law in consideration of the inertial resistance. Their empirical correction

$$C_D = \frac{24}{Re_d}\left[1 + 0.15\, Re_d^{0.687}\right]$$

is for $Re_d \leq 700$.

Ingebo[18] found that regardless of the magnitude of the particle acceleration, the drag data on solid spheres and liquid droplets could be correlated by the relationship

$$C_D = \frac{27}{Re_d^{0.81}}$$

for the Reynolds number range from 6 to 500.

A similar study performed by Langmuir and Blodgett[19] found that

$$C_D = \frac{24}{Re_d}\left[1 + 0.197\ Re_d^{0.63} + 0.0026\ Re_d^{1.38}\right]$$

best fit their data for $1 < Re_d < 100$.

Millikin[20] corrected the Stokesian law in consideration of rarefaction. His "general law of fall" is given by

$$F = 6\pi\mu r v\left[1 + (A_2 + Be^{-Cr/l})\,l/r\right]^{-1}$$

Carlson and Hoglund[21], using Millikin's law, determined the effects of rarefaction also. Their results are given by

$$C_D = \frac{24}{Re_d}\left[\frac{1}{1 + Kn\ (3.82 + 1.28\ \exp\ \frac{-1.25}{Kn})}\right]$$

Rudinger[22] determined the drag coefficient of accelerating glass beads in convective flow behind a shock wave. He found that all his data could be mathematically represented in the form

$$C_D = \frac{6000}{Re_d^{1.7}}$$

for $40 < Re_d < 300$. Rudinger believed that electric charges on the particles caused his data to deviate widely from the steady state drag curve for spheres.

Selberg[23] conducted an experiment similar to Rudinger and found that C_D varies considerably because of particle roughness. Using very spherical precision-lapped sapphire balls, his data did not produce the scatter as exhibited with particles having rougher surfaces.

Volume I of the Final Report on Contract No. NAS1-8708 is designated as NASA CR-66878, "Planetary Environment Simulation, Erosion and Dust Coating Effects."

2. PROBLEM DEFINITION AND APPROACH

2.1 DEFINITION OF PROBLEM. The present study is part of an investigation to study the causes and effects of a Martian sand/dust storm. This study is primarily concerned with an experimental determination of the drag coefficient and lift-to-drag ratios of small particles entrained in a simulated Martian wind. Additional work was undertaken to gain insight into single particle entrainment.

2.2 EXPERIMENTAL APPROACH. The objective in this study was to experimentally define the characteristic behavior of particles exposed to simulated Martian surface wind conditions. Simulation of Martian surface winds for the purpose of this study entailed generating wind speeds of up to 250 feet/sec in a static pressure range of 4 to 7 torr. This simulation was performed in the McDonnell Douglas Martian Environmental Simulator, which has a 9-1/2-inch by 14-1/2-inch test cross section. The wind tunnel produces an air flow with identifiable flow properties in the test section.

The study of small particle phenomena in low density high velocity air streams requires the following capabilities:

- Containment of particles in an identifiable flow.
- Ability to record particle flight paths.
- Sufficient particle path resolution to discern directional changes.
- A method for introducing particles into the air stream without imparting energy to the particle.

2.2.1 FACILITY DESCRIPTION. The wind tunnel is contained within a 9 x 11 x 20-foot high-altitude chamber, (Figure 2). The pumping system is a six-stage noncondensing type steam ejector which is used to maintain chamber pressure at values which simulate Mars surface conditions. Concurrently, air is metered into the stilling chamber where it then enters the tunnel nozzle to form a uniform and stable velocity profile in the test section. To improve the air velocity uniformity in the test section, two 20-mesh screens (with 0.016-inch diameter wires and 0.034-inch wide openings) separated approximately one inch are utilized in the stilling chamber to decrease the free-stream turbulence intensity. A typical velocity profile survey made with a traversing pitot-static probe is shown in Figure 3.

Air used for generating wind in the tunnel is drawn from the McDonnell Douglas Polysonic Wind Tunnel supply tanks. This air is dried to a dew point of -20 to -40°F. Variation in the combinations of wind velocity and chamber pressure are achieved by adjusting the metered air flow to the tunnel and throttling the chamber exit flow with the butterfly valve in the 30-inch diameter vacuum line leading to the steam ejector.

The test section for observing particle behavior is a glass and plexiglass tunnel 9-1/2 inches high by 14-1/2 inches wide by 36 inches long (Figure 4).

Free-stream air velocity in the tunnel is measured with a pitot-static probe (Figure 5). The differential which exists between the static and dynamic pressures is measured with a 1-torr (1 mm of mercury) range diaphragm-type electric manometer. Chamber static pressure is monitored with a 100-torr range unit. Copper-constantan thermocouples are used to measure temperatures at critical points in the air stream.

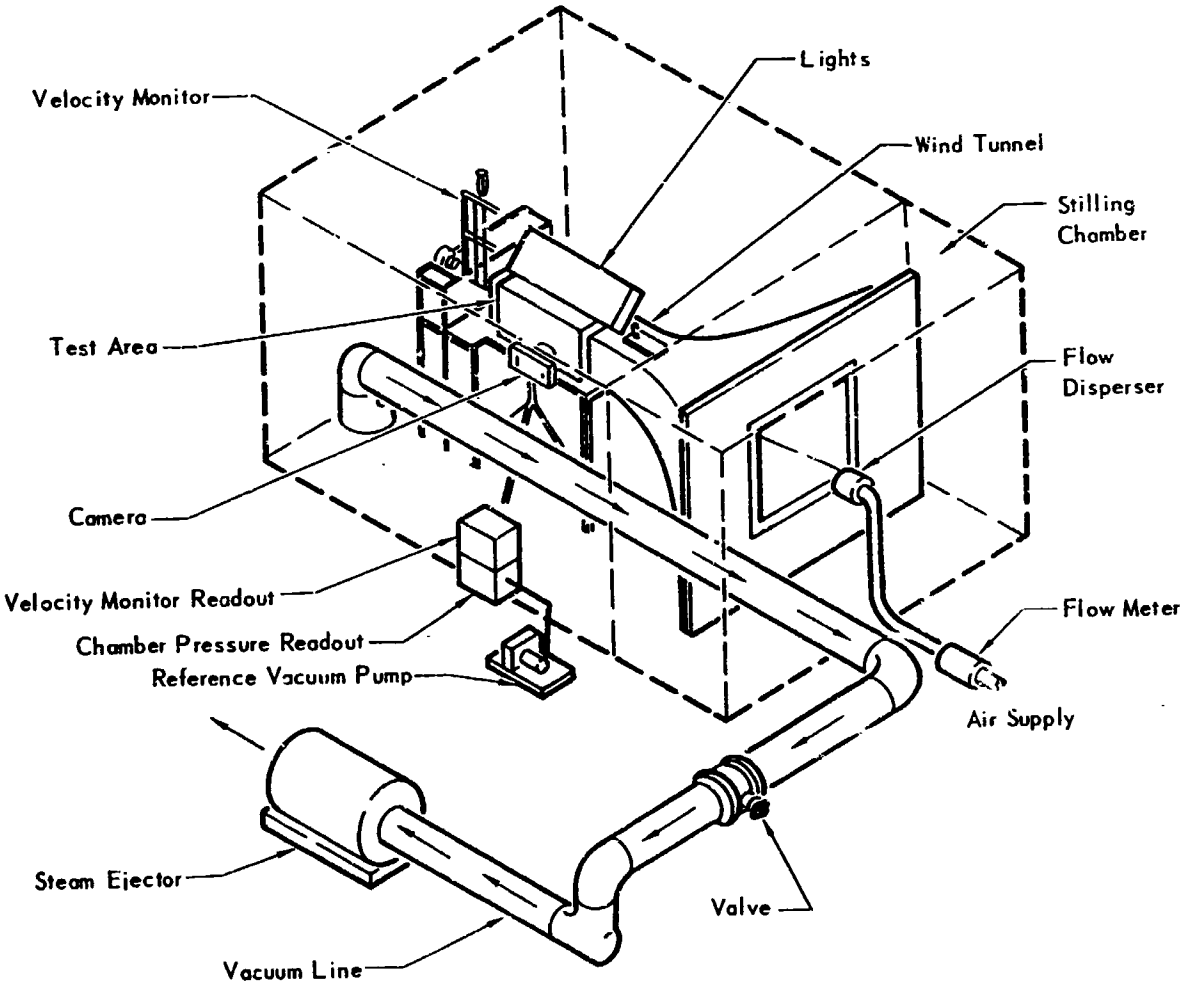

Figure 2 – McDonnell Douglas Martian Environmental Simulator

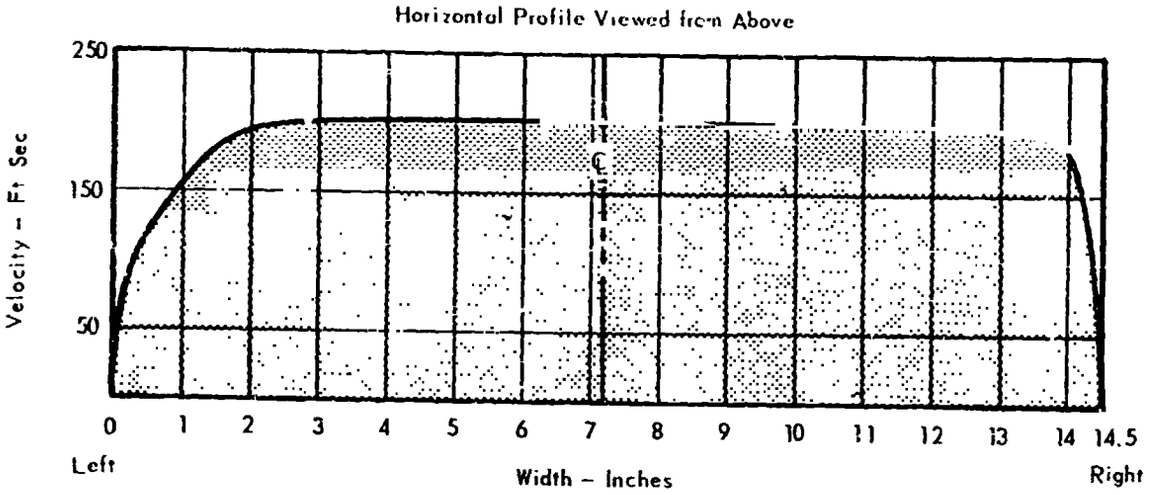

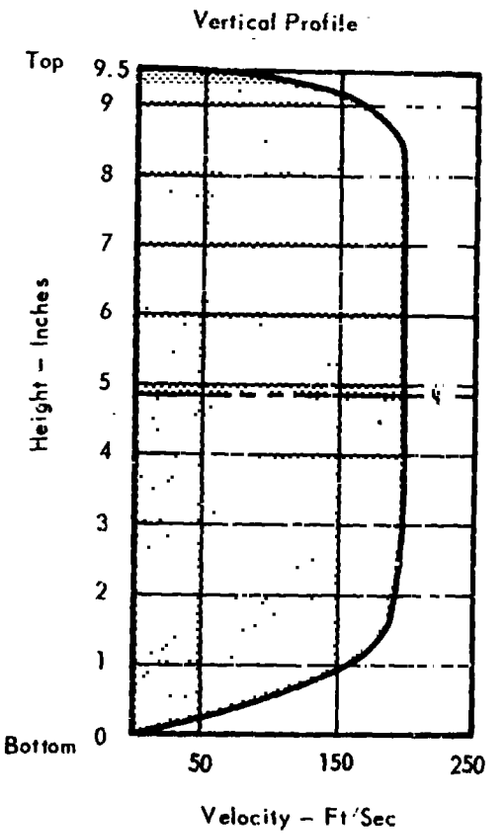

Figure 3 – A Typical Wind Velocity Profile at 9.5 Inch X 14.5 Inch Tunnel Exit

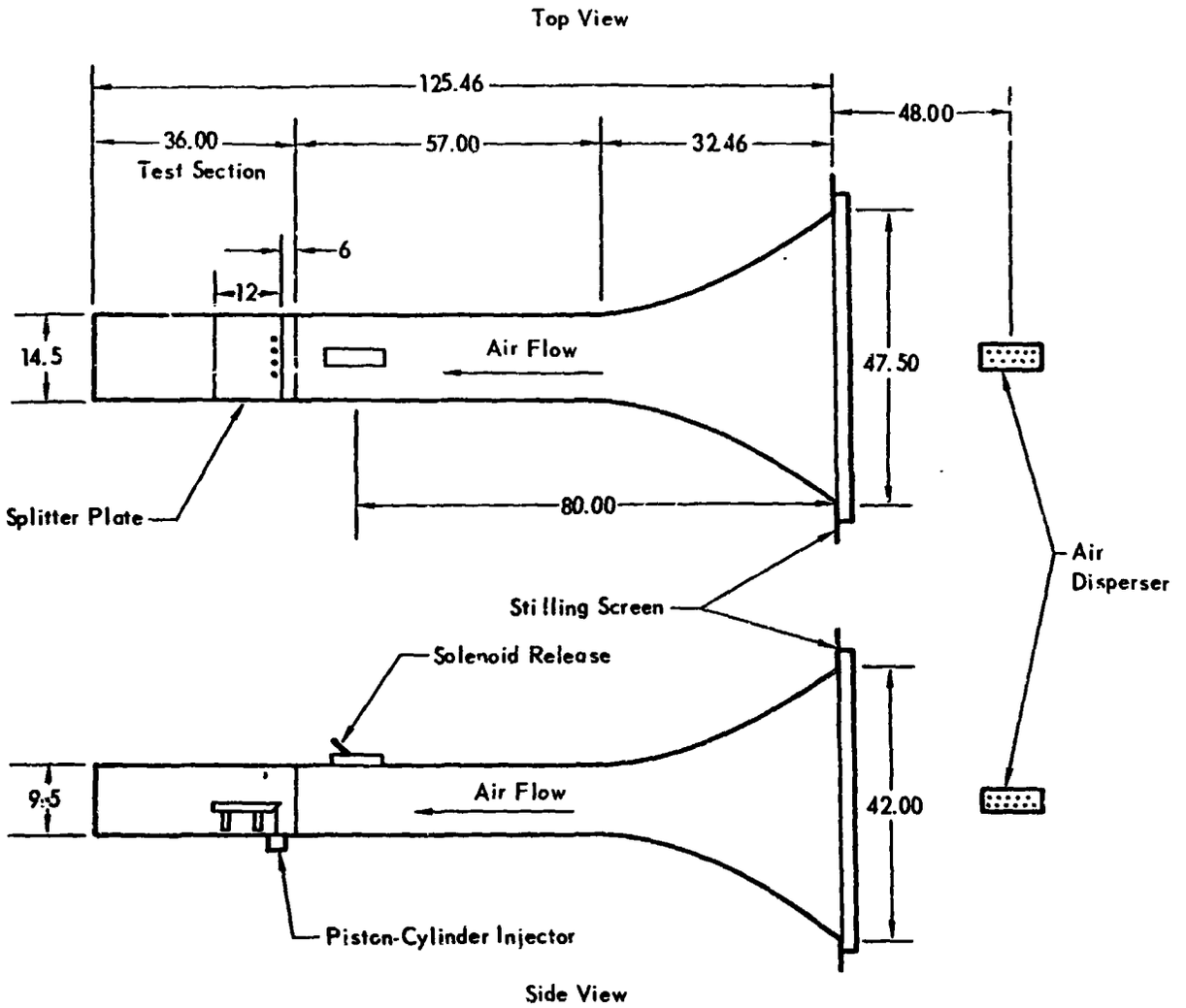

Note: All Dimensions are in Inches

Figure 4 – Wind Tunnel

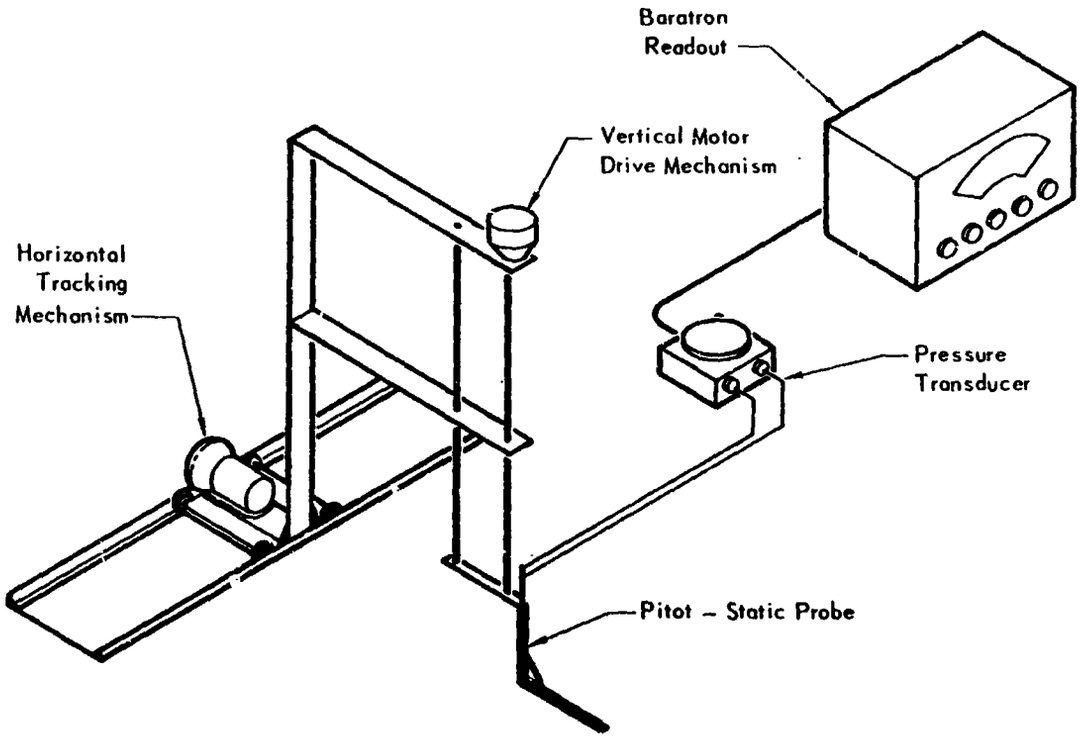

Figure 5– Velocity Monitor

2.2.2 PHOTOGRAPHY. The degree of accuracy in analyzing the behavior of a particle in the wind stream is dependent on the displacement versus time history for the particle. If this history is recorded by a photographic method, accuracy is limited by picture resolution. For this reason, several methods were evaluated on the basis of resolution. One method, holography, would provide a three-dimensional record of the trajectory during a continuous exposure. However, in order to obtain a large enough field of view, it would be necessary to enlarge the laser beam diameter with a lens, which would decrease its power per unit area. Since a laser which would provide the necessary power was not readily available, this technique was not used.

Another method, utilizing readily available equipment, is dark field photography. Initial investigations were made utilizing closed-circuit television monitoring and video taping of particle movements in order to optimize lighting arrangements, select particle sizes, and evaluate anti-reflection background materials. The video tape system consisted of a Coho Camera Model 2000, a Conrac Monitor Model CVA17, and Ampex Recorder Model VR7000. The camera scan was 525 lines/inch. The first lighting arrangement consisted of a 150-watt Xenon lamp built into a special light diffusing box which spreads the beam over approximately a one-foot wide field of view. This provided ample light to video-tape a fine stream of 100 micron sand particles, but failed to provide adequate light to track a single particle. In an attempt to view single particle motion, the Xenon lamp was replaced with two 500-watt mercury vapor lamps and the particle size was increased to approximately 500 microns. At low velocity (less than 10 ft/sec), these particles were just barely visible when viewed on the television monitor. It was felt that the lighting arrangement

and particle types had been optimized and that the television system did not warrant further investigation at this time.

Next, a Beattie-Coleman Type 14405 Polaroid Scope Camera and a Polaroid Model 250 camera were tested using 3000 ASA film. The same lighting was used as had proved best with the television system. Neither camera provided sufficient resolution to track particles smaller than 500 microns.

A Millikan Model DBM4C 16 mm framing camera was also evaluated with 400 ASA Kodak Linograph Shell-burst film. The camera was rewired for single frame, variable exposure operation. Lighting was the same as for the previous camera test. Initial tests indicated the need for better lighting and finer grained film for higher resolution. From experience gained in previous tests, a lamp housing was designed and built to collimate a beam of light to illuminate a long particle path with a minimum of reflected background light. The two mercury vapor lamps used in previous tests were replaced by four 1000-watt tungsten filament quartz envelope lamps for higher intensity. Initially, the lamp housing was positioned so that the collimated beam was perpendicular to the centerline (Figure 6a), to eliminate unwanted reflected light from the back wall of the test section. However, there was insufficient reflected light from the particles to produce good particle tracks on the film. Therefore, the lamp housing was repositioned so that the collimated beam was at a 45 degree angle to the camera (Figure 6b). In this configuration, which is the optimum arrangement for conventional photography, a greater amount of reflected light reached the camera, but excessive reflection from the test section back wall caused considerable "wash out" (loss of contrast). In addition it became evident after a number of runs that scratches caused by the abrading airborne

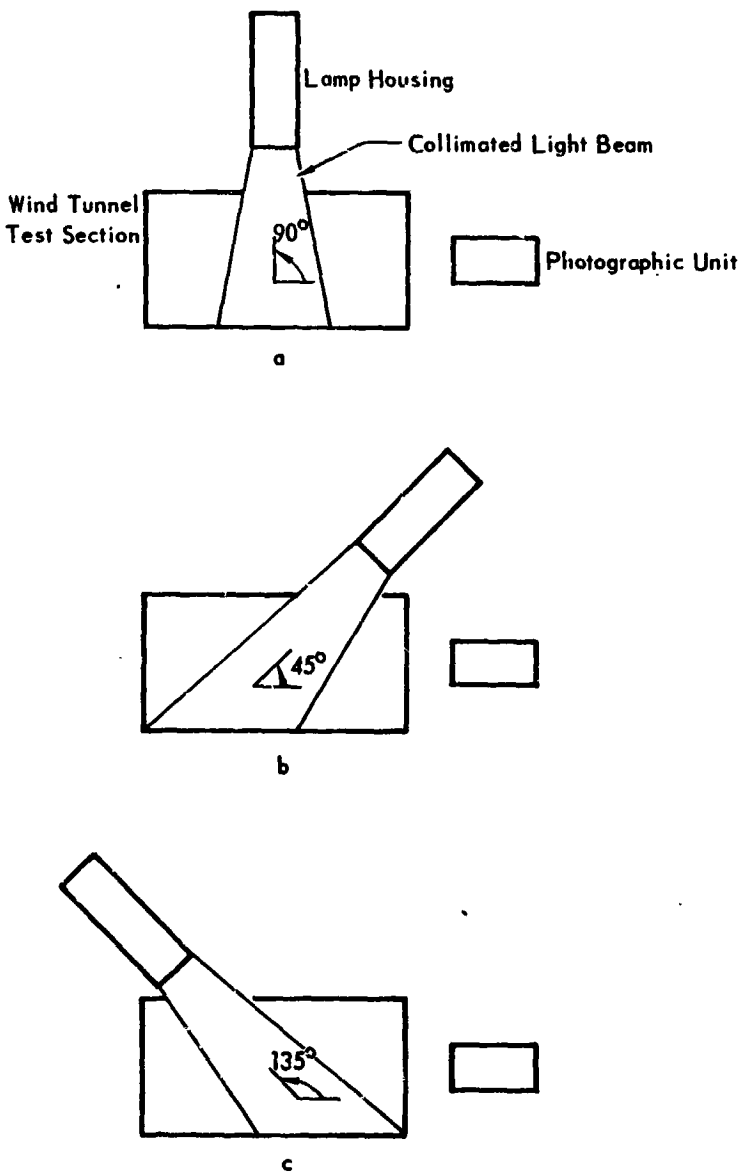

Figure 6 — Lighting Arrangements

particles plus the accumulation of a dust film on the near wall of the plexiglass test section was detrimental to particle resolution. Therefore, the all-plexiglass tunnel section was replaced with a glass tunnel section with a black-painted plexiglass bottom. The nonreflecting transparent back wall permitted light to pass through it and be absorbed by a black felt background located four feet behind the wall. The glass walls were less susceptible to scratches and accumulation of dust films. Tests with this tunnel showed that the amount of light reflected by particles smaller than 500 microns was still not ample for high-resolution pictures.

The lamp housing was repositioned so that the collimated beam made a 135 degree angle with the camera (Figure 6c). With this arrangment, the camera received more scattered than reflected light from the particles and the resulting resolution was improved for particles smaller than 500 microns. The best angle was that at which maximum forward scattering occurred without a direct beam shining into the camera lens. As a result, all subsequent particle track analysis was done using this lighting arrangement.

Although the Millikan 16 mm camera with Shell-burst film and the forward scattering light system provided reasonably good results, a Nikon 35 mm camera equipped with Panatomic-X film was tested and found to further enhance particle resolution. The photographic system ultimately selected for all subsequent track analyses was the Nikon 35 mm camera using Panatomic-X film, and the forward scattering light technique consisting of four 1000-watt tungsten filament quartz envelope lights positioned as shown in Figure 6c.

2.2.3 PARTICLE ENTRAINMENT. Before a displacement versus time flight history of a particle can be made, particle entrainment in the wind stream must be achieved. The introduction of particles into a wind stream must be controlled so that no energy, other than that which is imparted by the wind stream, can affect the flight history.

Three types of mechanisms were tested for this purpose. The first type of mechanism tested utilized a solenoid-actuated feed system which released particles from the top of the tunnel (Figure 7).

The second type of mechanism tested was an electrostatic particle release device. Its prime purpose was to see if actual "lift off" occurs from the floor of the test section. This type of mechanism provided a holding force on the particle and did not impart any movement to the particle when the force was released. Two closely spaced parallel plates were charged to a potential of approximately 1000 volts DC. The particles were then placed in the narrow gap between the ends of the plates where the electrostatic field provided a holding force. Although the device worked well in ambient air, the much lower dielectric strength of air at the test pressure of 6 torr resulted in corona discharge. The use of thicker insulation between the charged plates to overcome electrical breakdown reduced the electrostatic field strength and, consequently, the holding power of the device.

In spite of the problems with the electrostatic holding mechanism, some visual and photographic observations were made of particles released electrostatically. Visual coverage was enhanced by use of a telescope. No particles were observed to lift off the tunnel floor, but random rolling of particles was observed. The technique was eventually abandoned because of the erratic nature of particle departure from the holding device, and because particles frequently

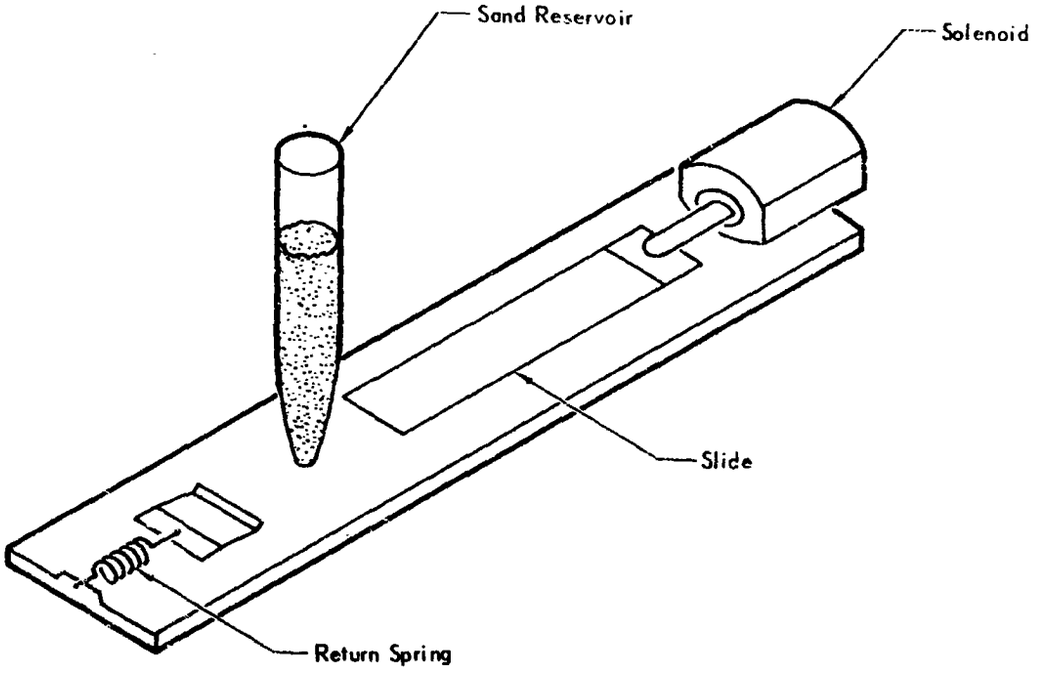

Figure 7 – Solenoid Particle Release Mechanism

would not roll even at wind velocities in excess of 250 ft/sec. It is suspected that stray electrostatic forces on the particles may have been responsible for the erratic particle behavior, although instrumentation used to detect stray voltages in the tunnel floor failed to indicate any such voltages.

The third type of mechanism tested was a piston-cylinder type device which pushed particles up through the tunnel floor (Figure 8). Its purpose was to determine whether particles of sand would "lift off" the test section floor. The mechanism was designed so that a slow continuous stream of sand particles could be extruded into the wind stream. This mechanism proved to be more successful than the electrostatic device and was used for all subsequent "lift off" experiments.

The solenoid-actuated feed mechanism, described first, was used in experiments for the determination of lift and drag forces on particles dropped into the wind stream.

2.2.4 COMPUTATIONAL PROCEDURE. Throughout the study of the motion of entrained particles in a simulated Martian wind stream, the drag coefficient and lift to drag ratio were determined from incompressible, two-dimensional, viscous air flow equations. The particle Reynolds number ranged from 2 to 11 for relative Mach numbers not greater than 0.2. The $M/Re_d^{0.5}$ values indicate that the air flow relative to the particles was in the slip-flow regime. However, the force-mass-acceleration technique used for determining forces on the particles, indirectly accounts for rarefaction and other body effects.

The following experimental variables are needed for analysis of the data in each run:

A. Flow Variables

1. Stream velocity

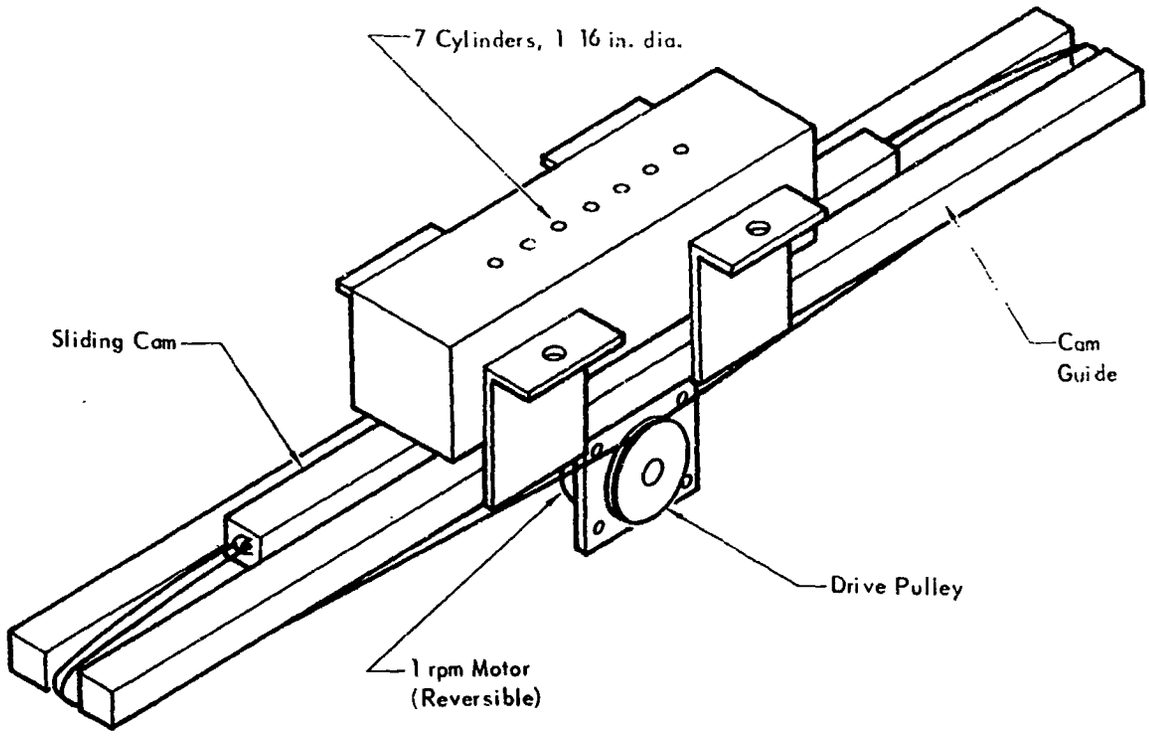

Figure 8 – Piston – Cylinder Injector

2. Gas viscosity

3. Gas density

B. Particle Variables

1. Diameter

2. Velocity

3. Acceleration

2.2.4.1 FLOW VARIABLES. At relatively low subsonic velocities where compressibility effects may be neglected, the free-stream velocity may be determined from Bernoulli's equation*

$$U_\infty = (2\Delta P/\rho_\infty)^{1/2} \tag{1}$$

The dynamic pressure, ΔP, was determined with a Pitot-static probe at tunnel center-line conditions. The flow density was determined from the perfect gas law

$$\rho_\infty = \frac{P_s}{RT} \tag{2}$$

for known tunnel pressures and temperature. The remaining flow variable, viscosity, was determined as a function of temperature from Sutherland's equation

$$\frac{\mu}{\mu_o} = \left(\frac{T}{T_o}\right)^{1.5} \frac{T_o+S}{T+S}$$

where the reference viscosity (μ_o) is 0.35×10^{-6} $\frac{lb_f\ sec}{ft^2}$ for reference temperature

* Symbols are defined in the list of nomenclature earlier in the report.

T_o = 492°R. The value of S is equal to 110.4°K.

2.2.4.2 PARTICLE VARIABLES. Throughout this study silica sand particles with an average bulk density of 1.51 gm/cm^3 were used (Figure 9). The particles were sieved to a 297 - 420 micron diameter range, and the mean diameter ($\bar{d}$ = 358 microns) was taken to be the representative particle size for use in data reduction.

The remaining important variables are particle velocity and acceleration. These parameters were determined from analysis of streak photographs of the displacement-versus-time history of the particles. The photographic equipment is shown in Figure 10. The stroboscopic effect of rotating a shutter disk in front of the camera lens made it possible to obtain the displacement-versus-time history of the accelerating particles. The shutter disk produced a constant exposure time of 2.82 milliseconds, as determined by monitoring the output of a photoelectric cell on a digital counter.

A typical flight path history of particles dropped from the ceiling mounted release mechanism into the test section is shown in Figure 11. The total displacements were resolved into x versus t and y versus t components. Either a finite difference table or a polynominal curve fit could be used to determine the particle velocities and accelerations. Since the difference technique represents an average velocity and acceleration, and is very sensitive to errors in displacement measurements, the curve fit technique was used.

For each particle track analyzed, at least six data points were used to fit a least squares curve to determine the motion of the particle. A second order polynominal fit implies that a constant force acts upon the particle. However, possible fluctuating wake phenomena and random body orientation of the

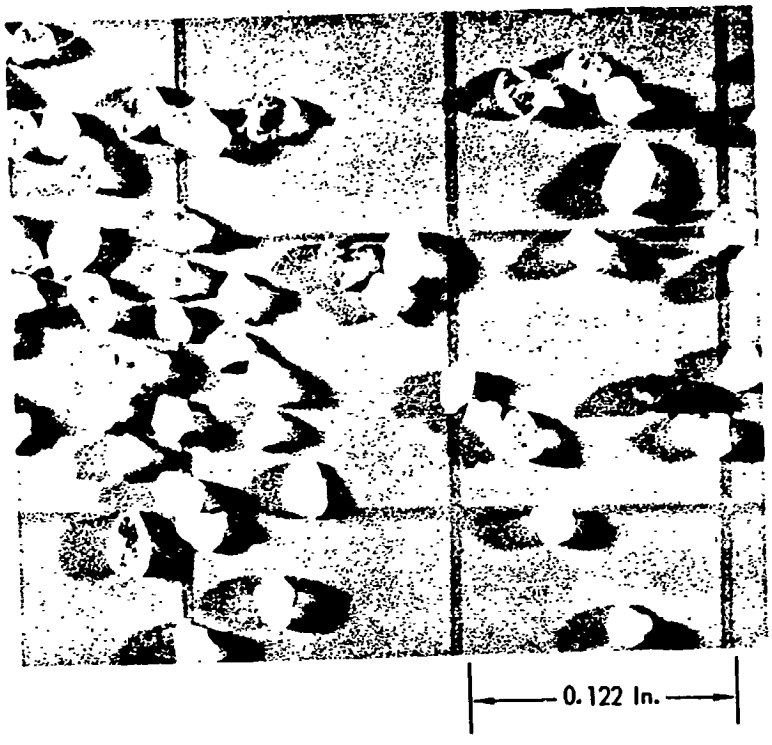

Magnification 12x

Analysis

Size μ	% Weight
> 358	60
< 358	25
385	15

Figure 9 – Photomicrograph of 297–420 μ Silica Sand

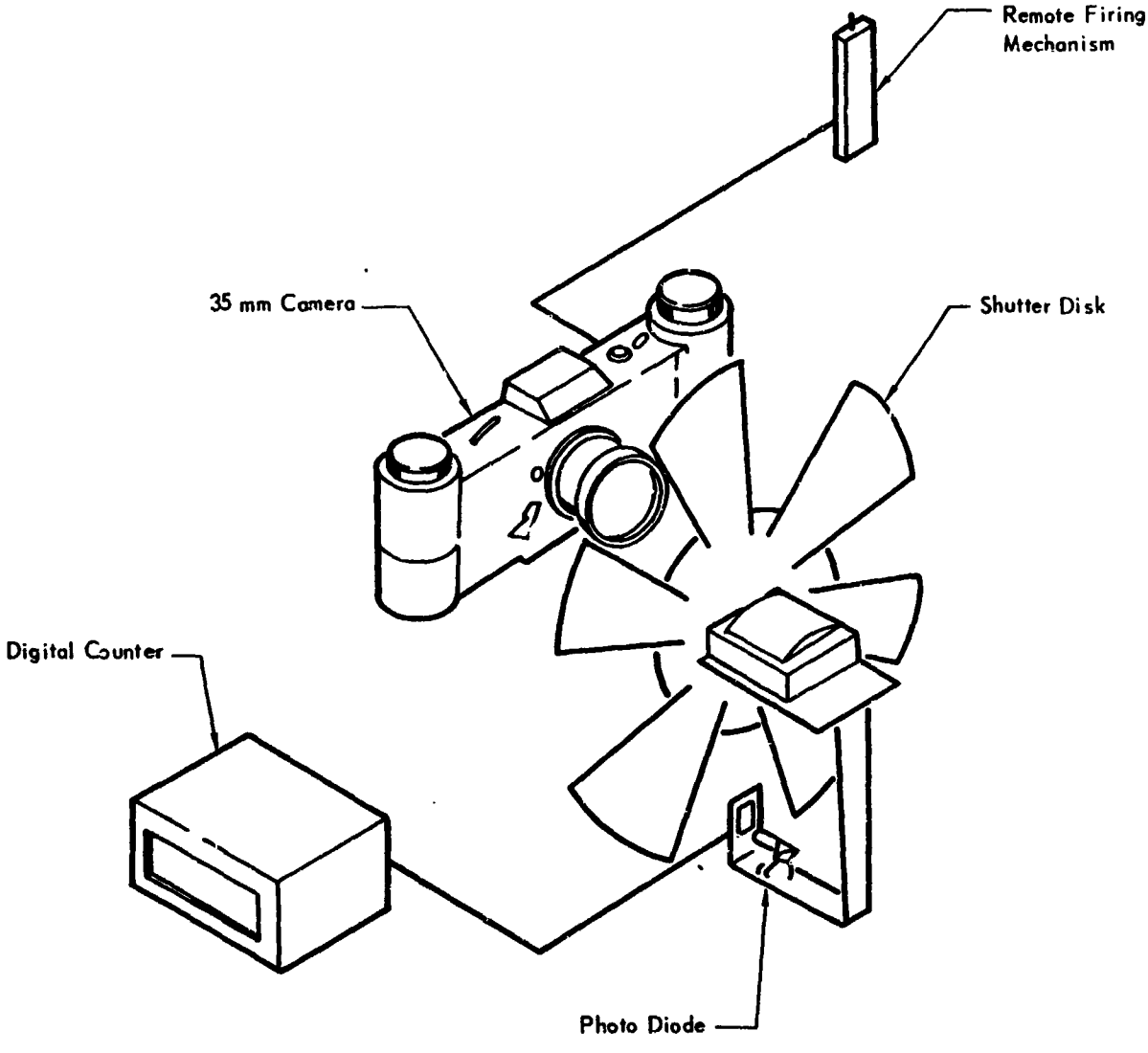

Figure 10 – Photographic Unit

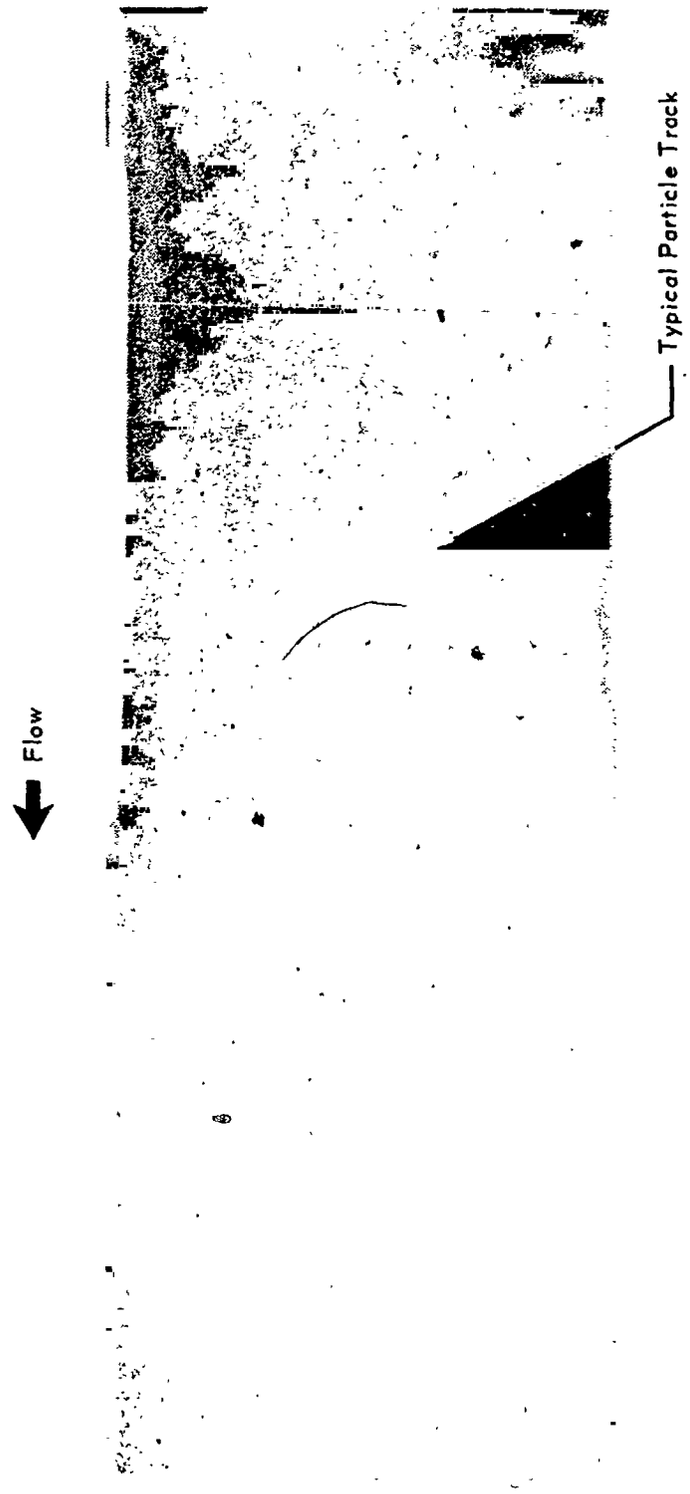

Note: Small circular spots are water spots due to film processing.
Large circular image is reflection of camera lens.

Figure 11 – Photograph of Typical Particle Entrained in 180 Ft/Sec Freestream Flow at P_s = 7 Torr

non-spherical particles will tend to impose varying forces on the particles. For these reasons, a third order polynominal was used to determine the approximate varying forces acting on the entrained particles.

Once the analytical expression for x versus t and y versus t are determined, the components of velocity and acceleration in an x-y plane may be obtained by differentiating the appropriate expressions. The mean flight time of the position data was substituted into the x and y versus t expressions to determine the instantaneous particle motion parameters.

Most of the data reduction was accomplished on a GE 420 Computer. For each particle track, the program calculated L/D, C_D, Re_d, an error analysis, and other pertinent information.

2.2.4.3 UNCERTAINTIES. Using the equations developed in Appendix A, a probable error analysis (Appendix B) was employed to obtain the propagating effect of errors in flow and particle parameters on the final answers. To help minimize these errors, the following restrictions were imposed on each experimental run and the resulting data:

- Tunnel flow parameters were stabilized before sand release and photography were started.
- Only distinct particle tracks were used.
- No particle track less than 15 diameters away from an adjacent track was used.
- To help eliminate wake effects, no particle aft of another particle in the same curvilinear track was considered.

The position data are conservatively estimated to have a deviation of less than 1/64 inch, including unavoidable errors in measuring particle

displacements and inherent errors in the photographic technique. However, small displacement deviations produce relatively large acceleration errors when double differentiation is performed on the analytical displacement expressions. The position data for 1/64 inch deviation were curve fitted to determine the uncertainties in particle acceleration and velocity. The uncertainties in the parameters needed to determine the particulate forces are listed below:

Parameter	Deviation
d	297 - 420 μ
P_s	0.01 torr
ΔP	0.001 torr
T	2°F
ρ_p	0.04 $\frac{gm}{cm^3}$
U_x, U_y	0.04 $\frac{ft}{sec}$
a_x, a_y	28 $\frac{ft}{sec^2}$

It is evident that the deviation in particle diameter and acceleration are the major contributors to the errors in this study. Since the probable error in C_D and L/D varies from run to run, a complete listing of the probable errors and other pertinent information is tabulated in Table 1.

2.2.5 PARTICLE FLUX COUNTING MECHANISM. Performance tests were conducted to determine the accuracy and sensitivity of a particle flux counting mechanism (Figure 12) developed at McDonnell Douglas, and to determine its response to

Table 1 – Data From Tests Using 297–420 μ Silica Sand

Point	Ps(torr)	U∞ (fps)	Up (fps)	Red	L/D	P(L/D)/(L/D)	CD	P(CD)/CD
1	5.70	163.90	18.25	7.57	.1762	.39	1.9200	.20
2	5.44	198.02	17.91	8.99	.0680	.14	1.1000	.18
3	5.44	198.02	19.48	8.91	.0694	.74	1.4700	.17
4	5.44	198.02	17.77	8.96	.0688	1.33	1.3650	.24
5	5.44	198.02	12.33	8.62	.1497	9.56	4.0400	.18
6	5.44	198.02	16.90	9.04	.4051	.61	2.0700	.20
7	5.44	198.02	21.48	8.81	.1011	.44	1.6300	.18
8	5.44	198.02	15.57	9.06	.0366	.52	1.3600	.23
9	5.44	198.02	20.58	8.86	.0711	.56	1.0420	.27
10	5.84	185.53	16.35	9.31	-.2018	5.84	3.9359	.19
11	5.84	185.53	22.17	8.99	-.0756	1.51	2.4421	.21
12	6.01	208.52	32.60	9.96	-.1097	1.26	2.7012	.22
13	6.38	132.61	12.10	7.16	-.0929	1.50	3.3877	.22
14	5.53	140.81	21.36	6.22	-.1077	1.76	2.9071	.26
15	5.53	140.81	27.12	5.92	.0388	2.99	5.2067	.21
16	5.58	185.53	24.04	8.98	-.1876	.87	1.7628	.24
17	6.01	208.52	25.82	10.34	.4250	1.52	.9273	1.43
18	6.27	206.16	27.60	10.73	.0829	1.42	2.8020	.21
19	6.27	206.16	21.28	10.81	-.0700	16.59	1.7462	.21
20	6.08	101.09	16.40	4.85	-.2450	.55	7.5482	.22
21	6.08	101.09	15.48	4.90	-.2400	1.19	3.4973	.33
22	6.08	101.09	16.52	4.84	.0336	7.21	3.9763	.30
23	5.60	58.76	10.91	2.49	.7042	1.08	5.4470	.65
24	5.37	81.77	12.16	3.47	.4182	10.73	1.3389	1.26
25	5.37	81.77	15.58	2.52	-.2153	.79	13.5688	.19
26	5.22	125.81	14.51	5.42	.0213	7.80	4.0370	.24
27	5.22	125.81	12.37	5.53	.1361	3.08	1.5586	.45
28	5.22	125.81	13.91	5.45	.2275	.90	3.3284	.26
29	6.38	132.61	19.16	6.74	.6654	.39	1.6990	.36
30	6.38	132.61	12.19	7.16	-1.0540	.77	-.5641	.58
31	7.84	61.41	9.08	3.79	-.9004	1.15	2.6462	.79
32	6.44	94.36	15.90	4.66	.3439	.93	3.6396	.35
33	6.68	135.15	16.80	7.30	-.0922	3.34	2.4370	.35
34	6.68	135.15	17.27	7.27	-.1188	3.40	1.8861	.44
35	7.13	179.95	20.28	10.52	-.0108	26.56	1.3468	.34
36	7.14	41.01	6.51	2.28	-.1821	2.78	10.3121	.51
37	7.17	139.06	31.11	7.14	-.4684	79	-4.3957	.38
38	7.17	139.06	27.16	7.41	-.2337	.74	-8.1979	.24
39	7.17	139.06	23.35	7.66	.3534	1.50	1.4620	.53

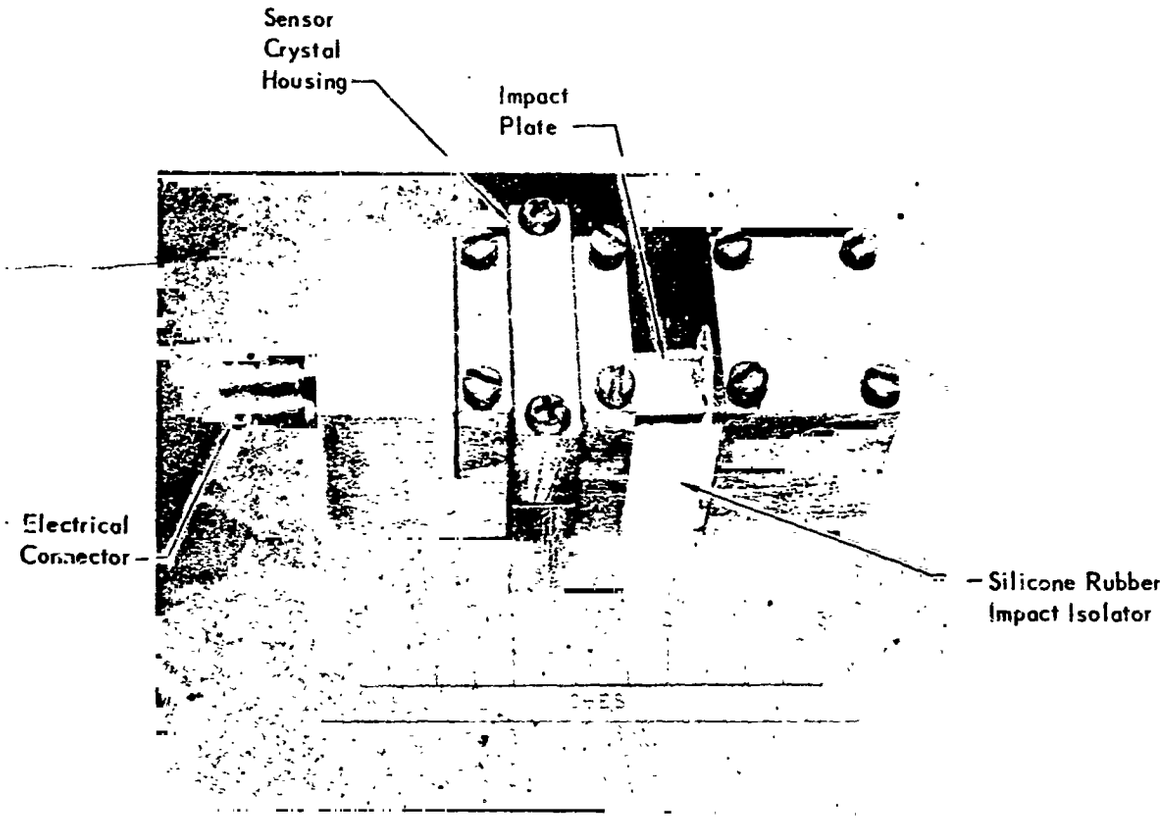

Figure 12 – Particle Counting Device

directional effects when exposed to simulated Martian environmental conditions. The particle counting mechanism utilizes a barium titanate sensing element. Preliminary studies indicated that the device is sufficiently sensitive to respond to the impact of a 100-micron diameter glass bead dropped from a height of two centimeters.

When a particle strikes the impact plate, a current pulse proportional to the particle momentum is generated in the barium titanate crystal. The pulse is amplified and sent into a threshold detector which differentiates between a true pulse and noise in the system. It was found that at a particular level of input momentum and amplification, the system gave a reasonably accurate count. However, when the amplifier gain was increased to distinguish particles of low momentum, mechanical resonance in the sensing element gave a false count when the sensor was struck by particles of higher momentum. Attempts to damp this resonance severely decreased the sensitivity of the system to the point where overall performance failed to meet expectations. It was felt that this system could not be relied upon to give an accurate particle count over a large momentum range and that the additional development effort which would be required to perfect the device was not justified at this time. Hence, the main effort of the overall program was directed toward the study of particle behavior, as described in the rest of the report.

3. DISCUSSION AND RESULTS

Experiments were performed on 297-420 micron particles to determine the forces imposed on these particles when subjected to an air flow that simulates hypothetical Martian surface pressure and wind velocity. Studies were conducted on particles entrained in the free-stream flow and on particles lying on a flat plate.

3.1 ENTRAINED PARTICLES. A free-flight technique was used to determine the drag and possible lift acting on a single entrained particle. The results are given in Figures 14 and 15. Particles were released into the free-stream flow from a solenoid-operated release mechanism in the tunnel ceiling. The dispenser was approximately 1.3 feet upstream of the test section where the particles were photographed.

The drag and lift on a particle will depend to some extent on the velocity lag of the particle with respect to the gas velocity. Gilbert, Davis and Altman[24] have demonstrated that a 297-420 μ particle has a significant velocity lag. The particle velocities in this study, which are in close agreement with their predictions, are between 8 and 16 percent of the gas velocity. See Figure 13.

To evaluate the significance of the drag data in Figure 14, it is necessary to understand the behavior of the flow with fluid-particle interaction. Although the data have a mean probable error of 24 percent, other naturally occurring phenomena may possibly be responsible for the scatter.

Above $Re_d \approx 0.1$ the ability to describe the flow field around a sphere either theoretically or empirically, decreases rapidly. The fluid flow around rough rounded particles (Figure 9), only approximates the fluid flow around spherical particles. The degree of particle roughness or irregularity probably has the most serious over-all effect on the flow field around a body. Body roughness directly affects the following interdependent characteristics: particle

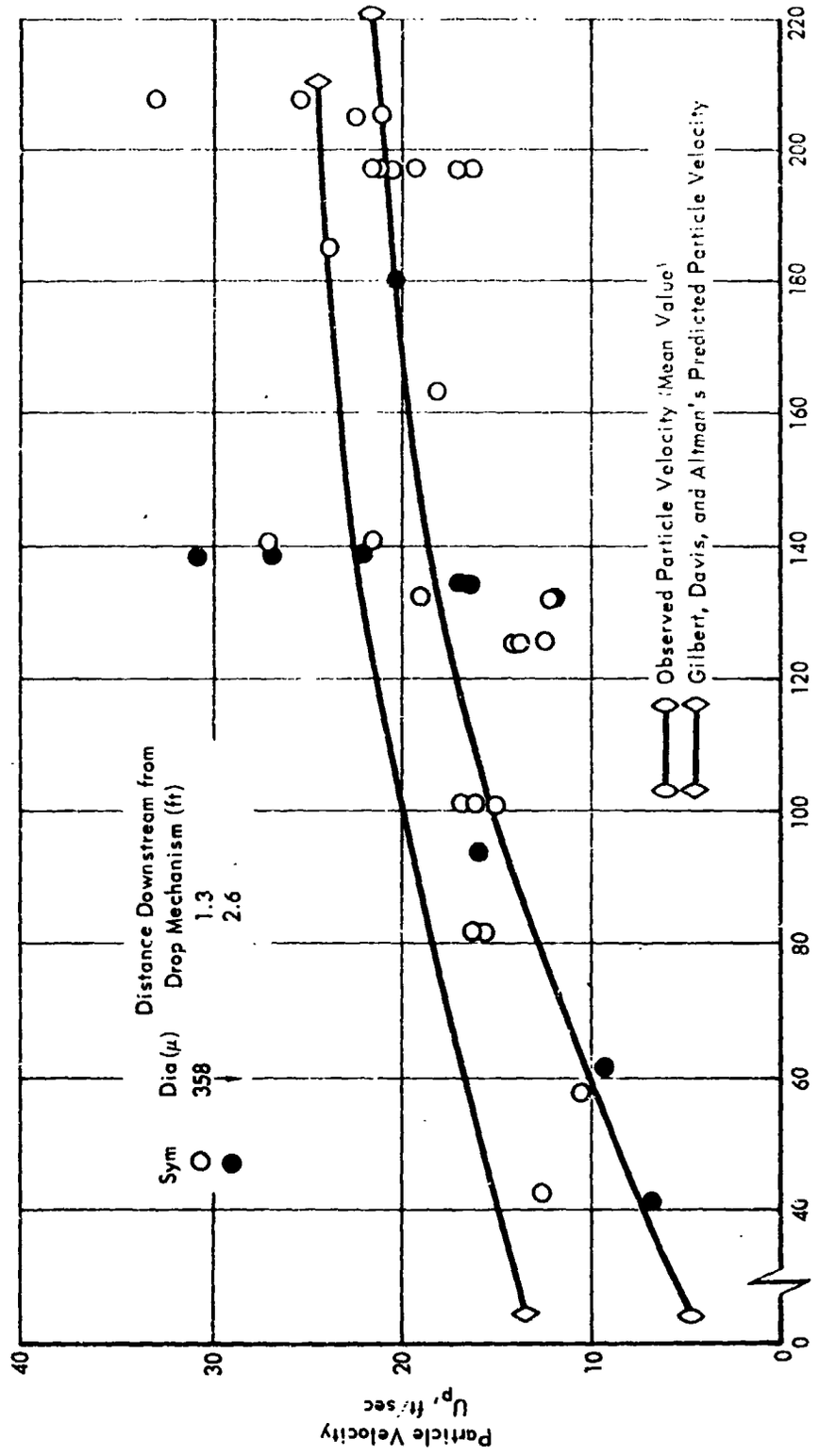

Figure 13 – Silica Sand Flight Velocity

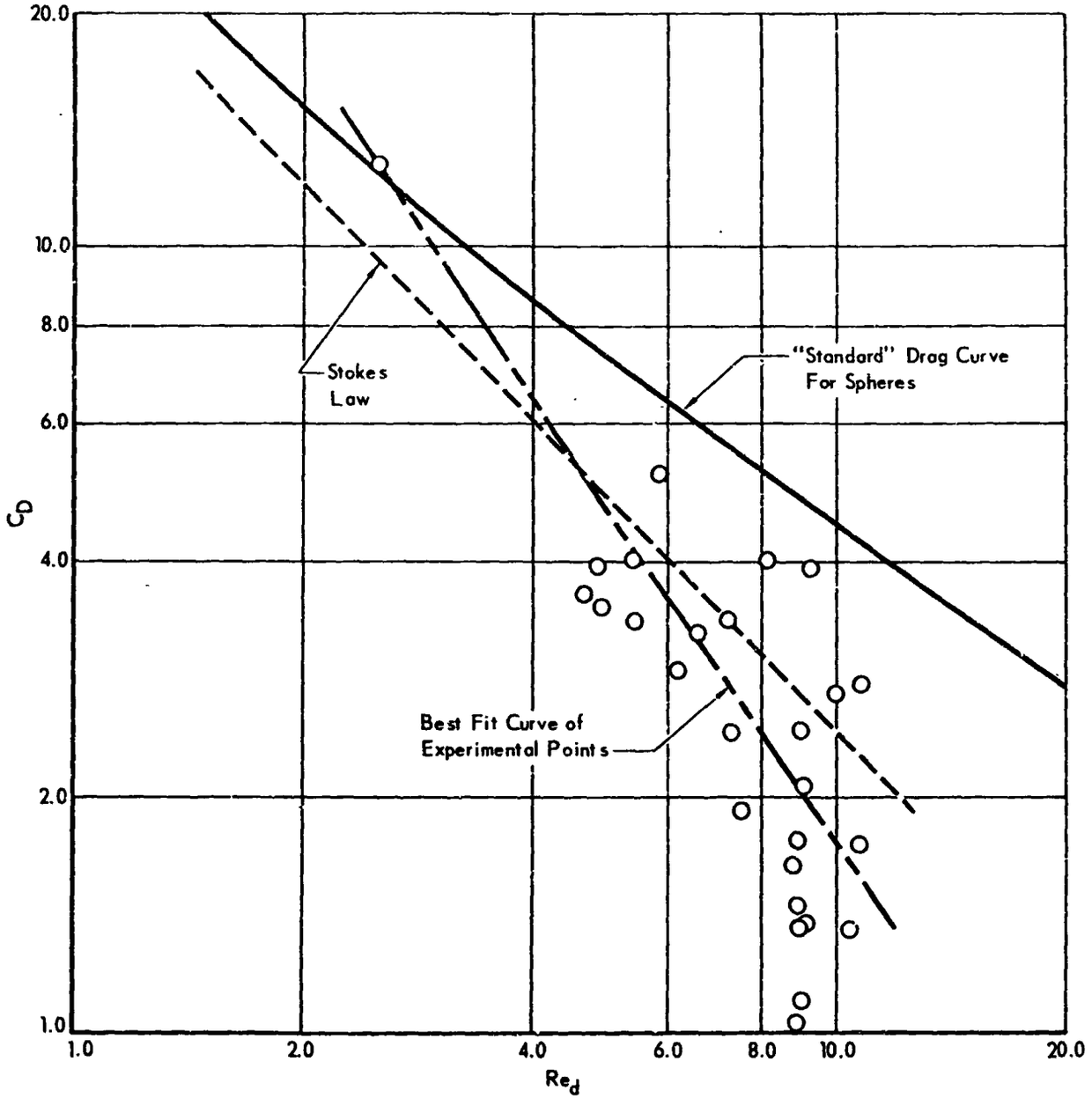

Figure 14 – Experimental Drag Coefficients

rotation and orientation in the flow, particle wake, and relative fluid turbulence.

Pressure and viscous forces will act on an irregularly shaped body in such a manner as to orient the particle to present the least aerodynamic resistance. Depending upon particle shape, this "streamlining" tendency can generate dynamic instability and possible particle rotation. The findings of Luchander[25] indicate that, below a critical Reynolds number, rotational effects have little influence on the drag coefficient of a single sphere rotating on an axis parallel to the flow. In the present study particle image resolution was insufficient to determine the orientation of the spin axis relative to the flow or even whether rotation occurred. However, in the gas flow around irregular bodies, it is possible that particle tumbling could substantially distort the symmetry of the particle wake and affect the relative gas turbulence.

When inertial and rotational effects prevent the fluid streamlines from closing behind a body, the streamlines curl up and form vortex rings. As the Reynolds number increases, the vortex rings grow in size and strength and eventually become unstable. New rings will form as the unstable ones detach from the body, so that the asymmetrical wake flow becomes periodic. Nisi and Porter[26] have clearly shown that this phenomenon occurs at Reynolds numbers as low as 8.1. The great degree of scatter in the experimental drag (Figure 14) for Reynolds numbers from 8 to 10 may be attributed to this phenomenon. Lunnon[27] remarked that there should be a periodic increase and decrease in the drag coefficient corresponding to the alternate growth and slipping away of the vortex rings.

Surface roughness causes an early transition in the boundary layer on a body.[28] The resulting turbulent flow in the particle wake along with any initial free-stream turbulence will act to increase the relative turbulence

intensity in a solid-gas flow system. Torobin and Gauvin[16] have studied the effects of turbulence on the drag coefficients of accelerating spheres. For a low free-stream turbulence intensity, they were able to attain relative turbulent intensities of the order of 40 percent for a solid-gas flow. Their drag data indicate a characteristic sharp drop in the momentum transfer at sufficiently high turbulence intensities. For each intensity level, the drag coefficient varied from 1 to 0.1 for Reynolds numbers from approximately 600 to 3000.

Other factors can influence the magnitude of forces acting on freely moving bodies. Rarefaction effects must be considered when the mean free path of the gas molecules is comparable to the dimensions of the particle boundary layer. Whenever the value of $M/Re_d^{0.5}$ is greater than 0.01, the relative flow is considered to be rarefied. The data in this report were obtained in the slip flow regime, $M/Re_d^{0.5} \approx 0.04$. Based on the results of Millikan's oil drop experimentation,[17] the net effect of rarefaction is to decrease the momentum transfer.

Bugliarello's studies[29] of accelerating spheres indicate that the drag coefficient is dependent upon the acceleration modulus $\frac{a_d}{U_p^2}$. Torobin and Gauvin[16] concluded that "an increase in wake turbulence resulting from Reynolds number increase or from the occurrence of surface roughness seems to diminish the acceleration effects." Since the acceleration modulus is essentially zero and the relative turbulence intensity is probably high in our wind tunnel, it is felt that acceleration effects are negligible in our work.

Most investigators neglect lift forces when studying accelerating particles entrained in a gas flow. In this study an attempt was made to determine if this assumption is valid. The accuracy in determining the small y-component of

acceleration was seriously hampered by an unavoidable 26 ft/sec^2 deviation due to limitations of particle track recording and measurement. Error analysis indicates that the resulting probable error in lift is too high to permit accurate determination of L/D values. The L/D data in Figure 15 fluctuate about 0.02 with an essentially equal number of positive and negative values. Studies by Maccoll[30] and others[31] have also found that negative lift can occur and is strongly dependent upon the type of flow and the degree of asymmetry in the wake structure.

3.2 FLAT PLATE. Several experiments were conducted to determine the process of particle entrainment (pick up) from a flat surface. The analytical problem is complicated by the complexity of the fluid-particle interaction in the flow structure beneath the boundary layer. Consequently, no analytical treatment was attempted and only the observable phenomena will be reported.

Initially, a few silica sand particles (297-420 microns) were distributed on the tunnel floor and exposed to a 200 ft/sec gas flow. No movement was directly observable in the viscous sublayer of the relatively thick boundary layer. However, when particles were released from the ceiling to simulate saltation, the particles impinging on the layer of sand on the tunnel floor produced enough turbulence and collisions to start a chain-reaction erosion process of the layer of sand on the tunnel floor.

Next, a flat plate with its upper surface polished to a 30 micro-inch finish and its leading edge beveled, was installed on the tunnel centerline to provide a supporting surface with only a thin boundary layer relative to the particle diameter (Figure 16). The piston-cylinder injectors, 1 inch apart and located 0.015-inch aft of the sharp leading edge, were used to slowly inject

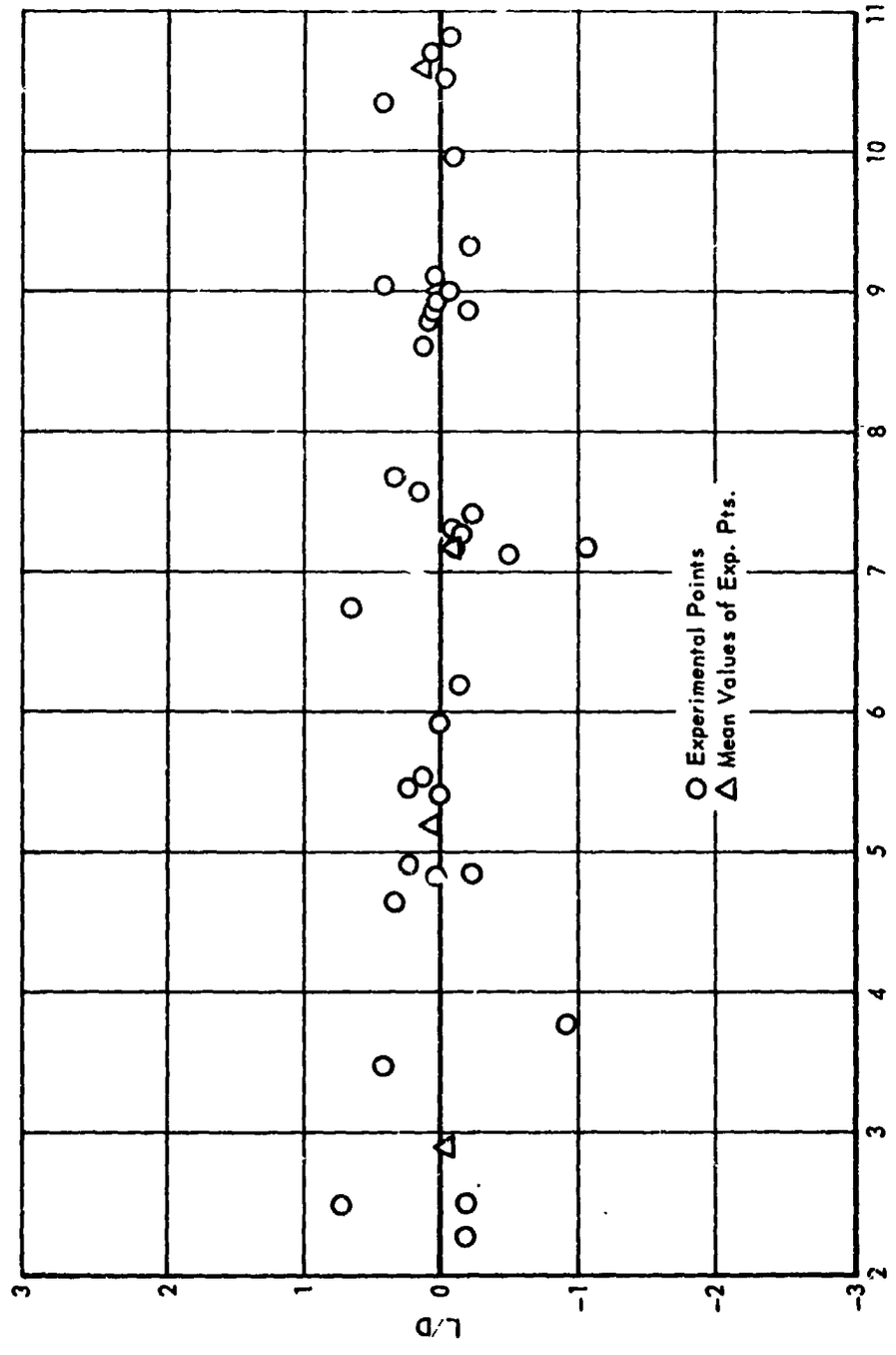

Figure 15 – Lift to Drag Ratios for all Data Using 297–420 μ Silica Sand

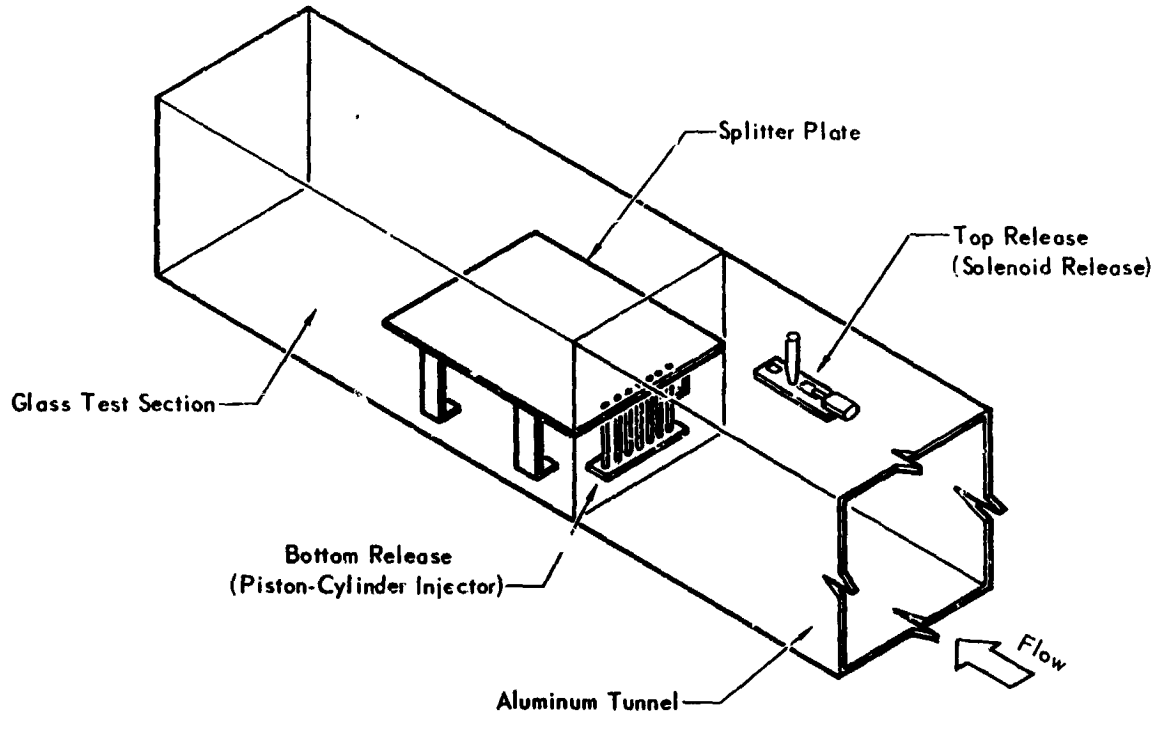

Figure 16 – Release Mechanisms With Splitter Plate

approximately 50 particles (297-420 microns) from each cylinder onto the upper surface of the flat plate. Particle reaction to the air stream was intermittent as the pile formed. The particle piles probably caused local turbulence and thus precluded the possibility of studying the observed phenomena as indicative of isolated particles.

Next, a few particles were randomly distributed on the plate to determine the free-stream velocity necessary for movement of an isolated particle. During the usual observation time, no observable movement occurred for velocities less than approximately 170 ft/sec. Depending possibly upon particle shape, intermittent and continuous movements were found to occur for free-stream velocities from 170 to 230 ft/sec. Some particles would move downstream for approximately 2 inches while other particles would roll continuously off the plate. However, no particles were observed to achieve entrainment. In this velocity range it is hypothesized that microscopic eddies are of sufficient strength to penetrate the viscous sublayer and induce movement of the surface layer of grains. As can be seen in Figure 17, a turbulent eddy in a high velocity stream would have a greater chance of penetrating the laminar sublayer and, consequently, reaching the surface than it would at a lower velocity. At the lower velocities, it is believed that the strength of a turbulent eddy is greatly dissipated in the thick sublayer and is insufficient to generate a critical surface disturbance necessary for particle movement.

For free-stream velocities near 230 ft/sec, particles achieving entrainment were observed (Figure 18). Photographic analysis in conjunction with visual observations of the sand particle behavior on the flat plate showed three basic types of response: (1) no movement, (2) movement along the surface in straight lines parallel to the direction of flow (it is assumed that these particles

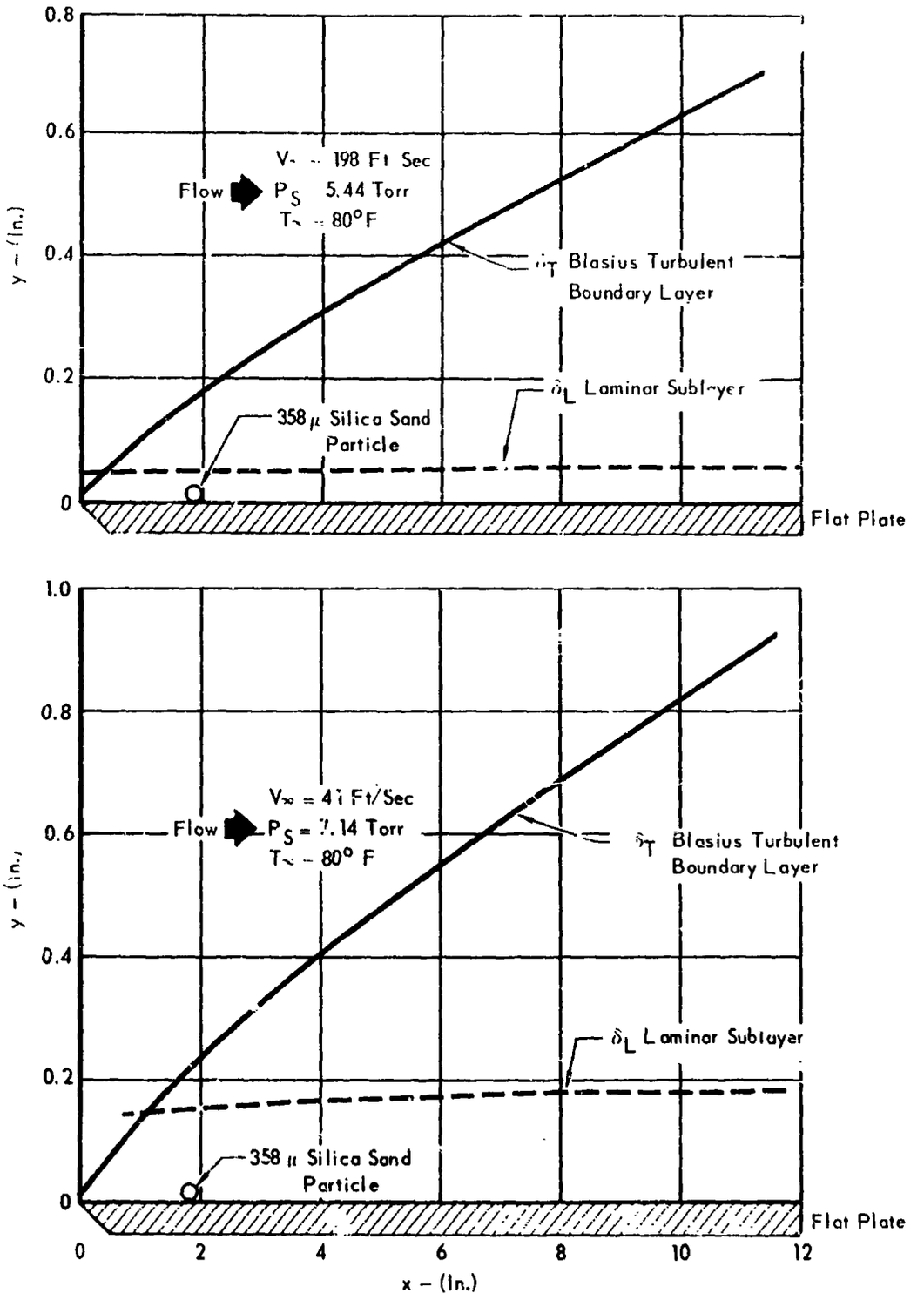

Figure 17 – Flat Plate Boundary Layers

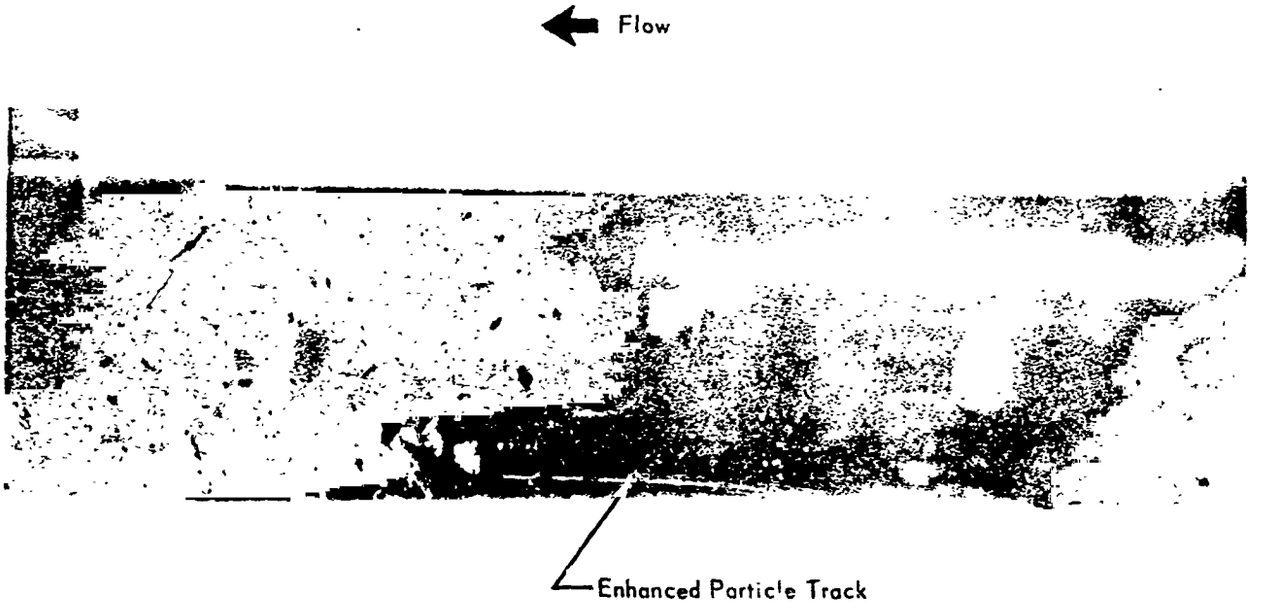

Figure 18 – Isolated Particle Entrainment from a Flat Plate in 230 Ft/Sec Free Stream Flow at P_s = 6 Torr

rolled), and (3) particle entrainment.

The particles that "rolled" presented an interesting phenomena. It was a characteristic of these particles to continue down the plate with short, convulsive movements. The particles stopped and started several times. This could be explained by local turbulences in the boundary layer.

The particles that achieved entrainment did so by preliminary particle interaction. That is, entrainment was preceded by a "roll" or a collision. No particle was observed to "lift-off" by the action of the gas flow alone. Collisions were of two types: (1) a "rolling" particle hitting a stationary particle and (2) a previously entrained particle hitting a stationary particle. Both types caused particle entrainment; however, it was not readily discernible which of the colliding particles was entrained. The rolling particles achieved entrainment after having rolled between 1 and 4 inches. It is believed that their irregular shapes induced a "bounce" which initiated entrainment.

After the isolated particle observations were made, a 1/4-inch deep bed of sand particles ranging from 297 to 420 microns in diameter was placed on the flat plate and exposed to a simulated Martian wind.

No observable movement occurred for free-stream velocities less than 180 ft/sec. Intermittent and continuous movement occurred from 180 to 245 ft/sec, and saltation over 245 ft/sec. Several photographs are presented in Figure 19. As can be seen, the saltation intensity fluctuated with time. This may have been the result of local flow variations or bed streamlining during the exposure. After several minutes, the flow was terminated and the bed inspected. Erosion to the leading edge and a "smoothing" of the bed surface was observed. No attempt, however, was made to determine the amount of erosion.

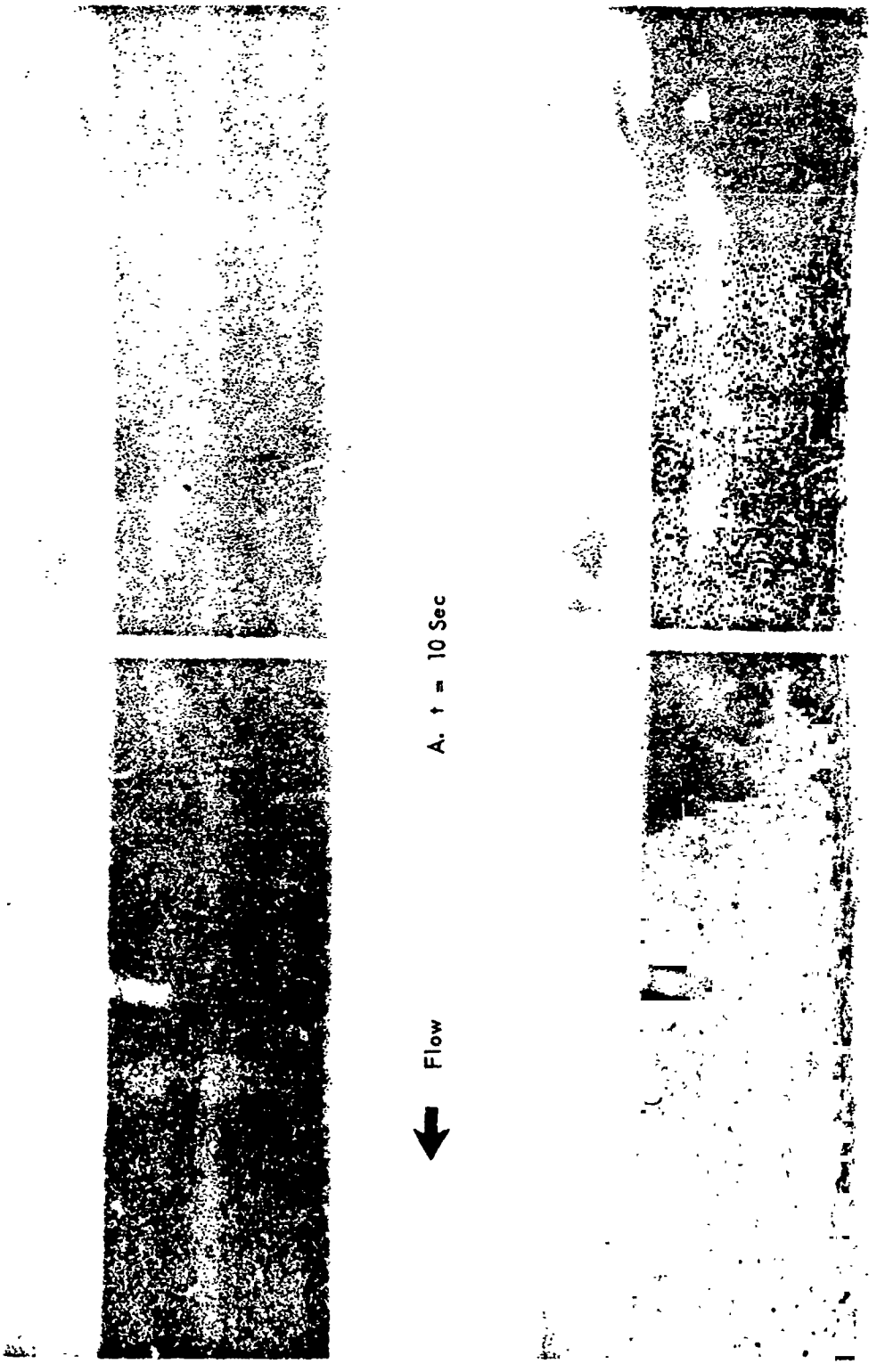

NOTE: t = 0 Corresponds to Incipient Saltation.

Figure 19 – Saltation on a Flat Plate in a 247 Ft/Sec Free Stream Flow at P_s = 5 Torr

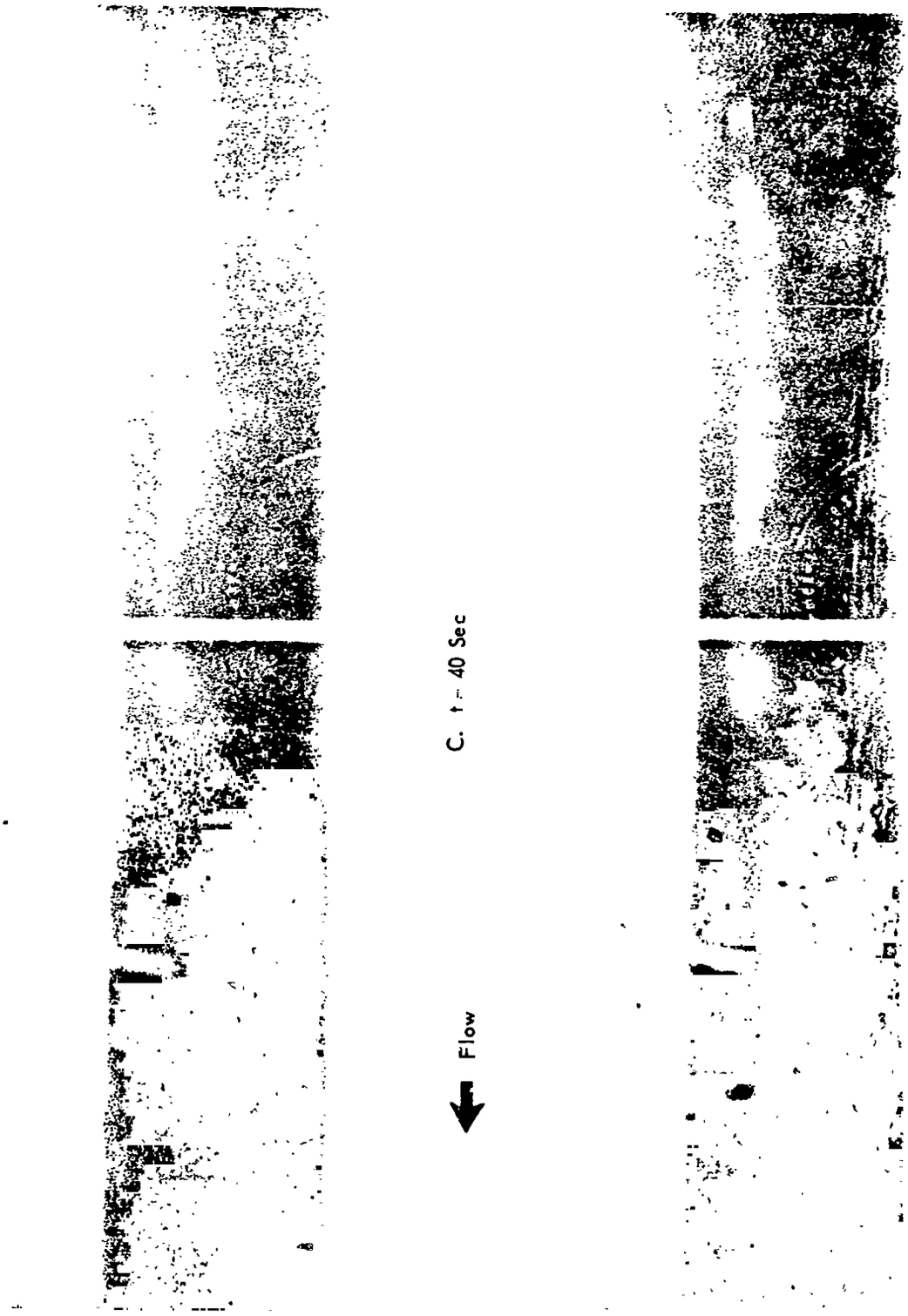

NOTE: t = 0 Corresponds to Incipient Saltation.

Figure 19— Saltation on a Flat Plate in a 247 Ft/Sec Free Stream Flow at P_s = 5 Torr (Continued)

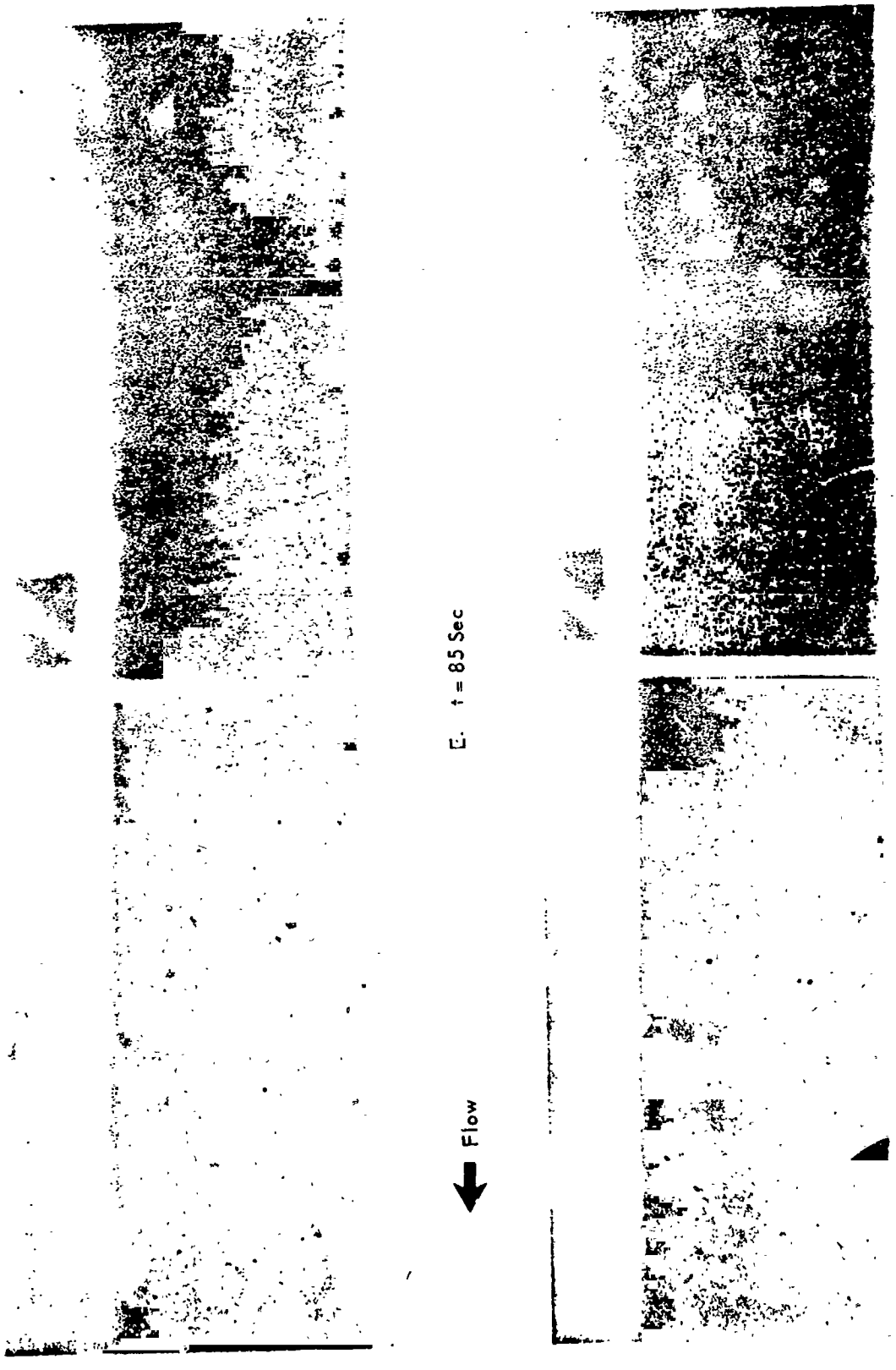

NOTE: t - 0 Corresponds to Incipient Saltation.

Figure 19 – Saltation on a Flat Plate in a 247 Ft/Sec Free Stream Flow at P_s = 5 Torr. (Continued)

Upon completion of the above, the bed was exposed to a second gas flow and the same particle movements observed during the first exposure (Ref. Figure 19) was observed for approximately the same free-stream velocities. See Figure 20. Additional erosion to the leading edge and bed surface was also observed.

3.3 CONCLUDING REMARKS. Observations made during the study of silica sand particles ranging from 297-420 microns in diameter are summarized below:

(1) The particle velocity is approximately 8 to 16 percent of the gas velocity.

(2) Instantaneous lift to drag ratios of entrained particles varied from +1 to -1 with an average L/D value of +0.02.

(3) Drag coefficients for particles with Reynolds numbers from 4 to 10 are generally lower than Stokesian values.

(4) No movement occurs for isolated particles on a flat plate exposed to gas flows ranging from 0 to 170 ft/sec.

(5) Intermittent and continuous "rolling" occurs for isolated particles on a flat plate exposed to gas flows ranging from 170 to 230 ft/sec.

(6) Entrainment and convulsive "rolling" occurs for isolated particles on a flat plate exposed to gas flows over 230 ft/sec.

(7) Entrainment is a saltation process.

(8) No movement occurs for a bed of particles on a flat plate exposed to gas flows ranging from 0 to 180 ft/sec.

(9) Intermittent movement occurs for a bed of particles on a flat plate exposed to gas flows ranging from 180 to 245 ft/sec.

(10) Saltation occurs for a bed of particles on a flat plate exposed to gas flows over 245 ft/sec.

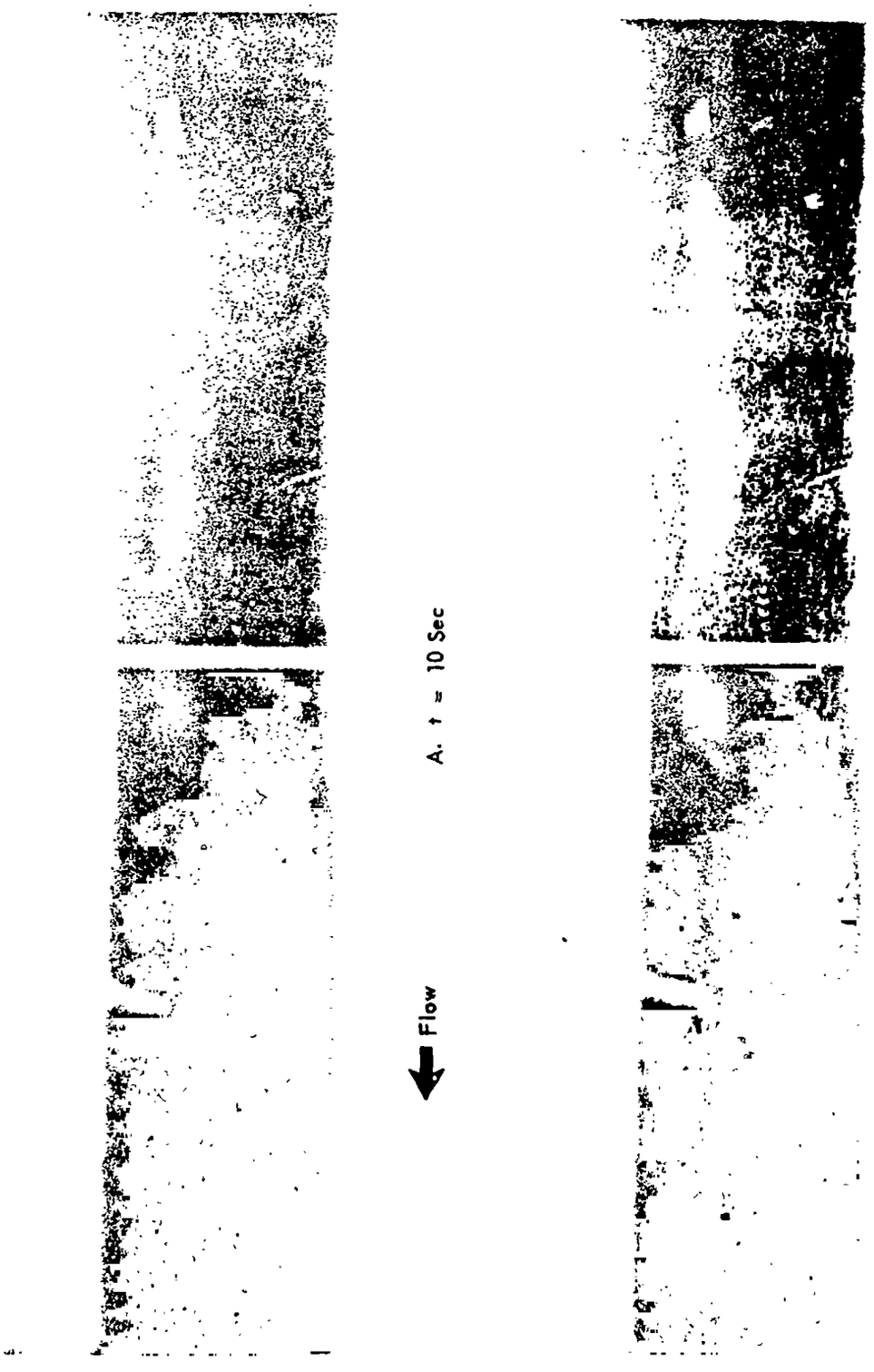

NOTE: t = 0 Corresponds to Incipient Saltation.

Figure 20 – Saltation on Flat Plate in a 248 Ft/Sec Free Stream Flow at P_s = 6 Torr.

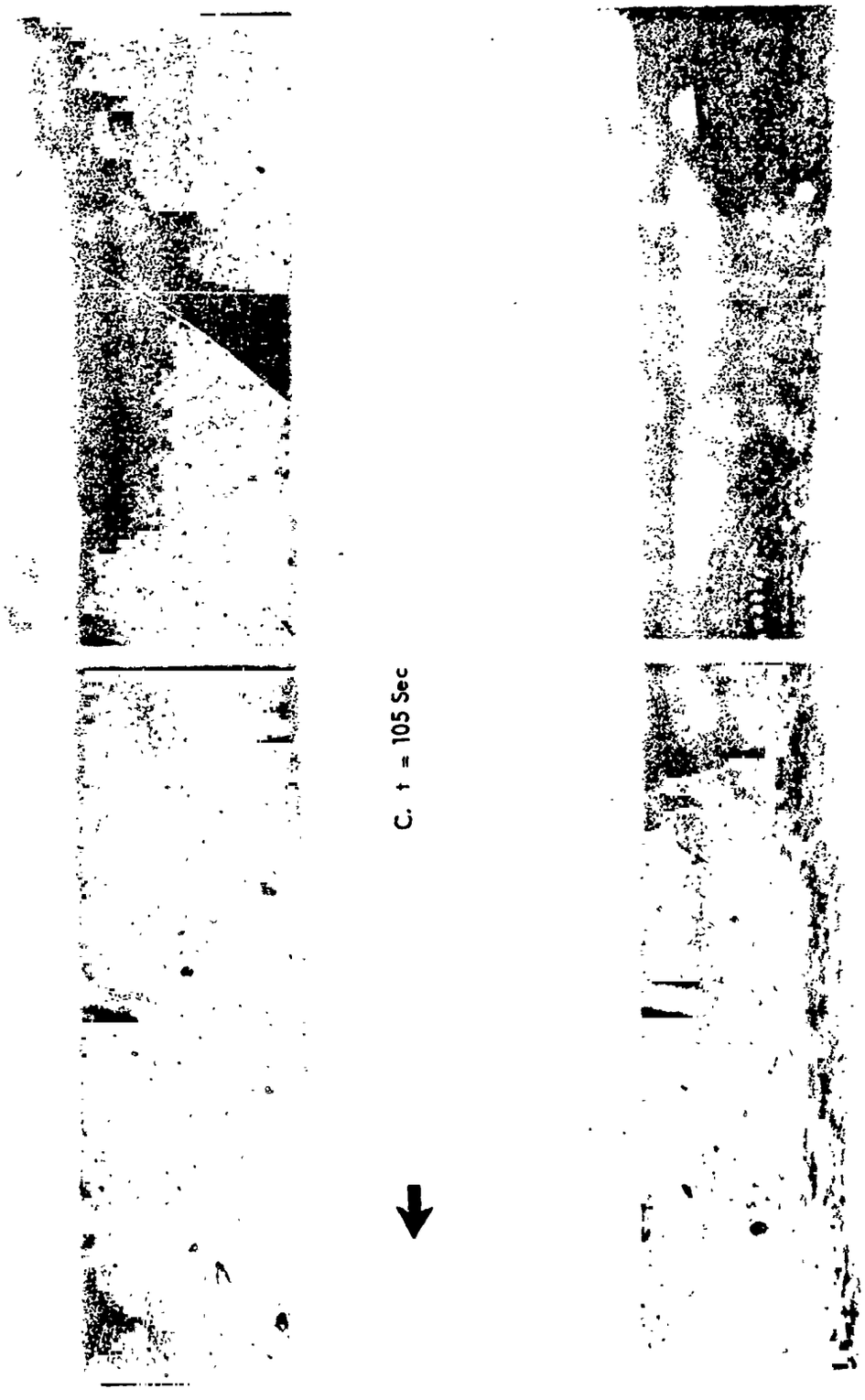

NOTE: t = 0 Corresponds to Incipient Saltation.

Figure 20 – Saltation on Flat Plate in a 248 Ft/Sec Free Stream Flow at P_s = 6 Torr. (Conuinued)

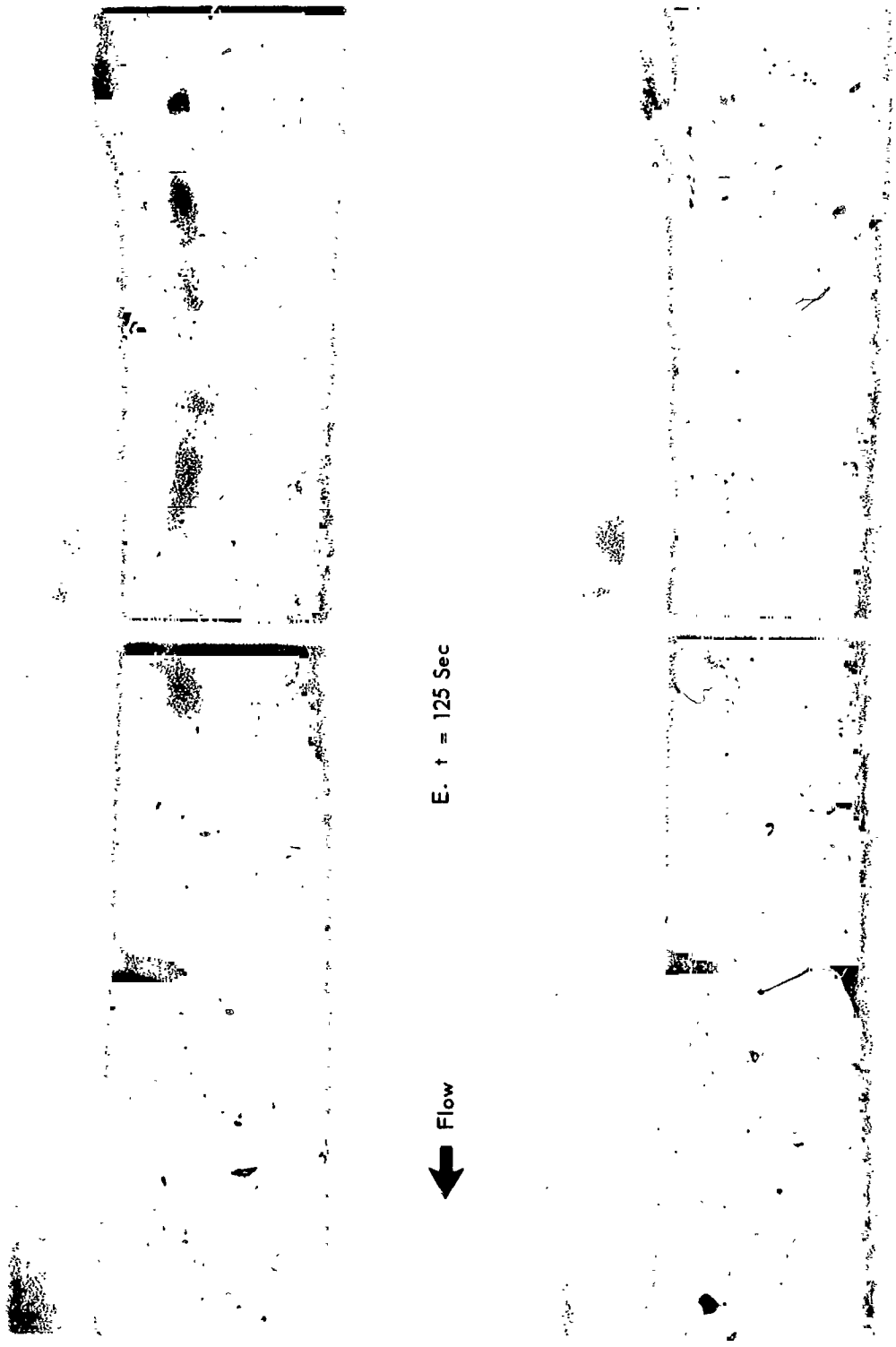

NOTE: t = 0 Corresponds to Incipient Saltation.

Figure 20 – Saltation on Flat Plate in a 248 Ft/Sec Free Stream Flow at P_s = 6 Torr (Continued)

This study has only touched upon the behavior of particles under a simulated Martian wind. Much work is left to be done on particle drag coefficients, lift-to-drag ratios, momentum transfer, and entrainment.

4. RECOMMENDATIONS

It is recommended that the work described in this report be continued. Specifically, the following investigations are recommended:

1. Determine the effect of particle size, density, and free-stream velocity on the momentum transfer of spherical particles in simulated Martian surface wind conditions. The forces acting on an entrained particle depends significantly upon the particle velocity relative to the free-stream flow. Recent in-house experiments indicate that irregularly shaped 500 μ particles achieve only 10 - 15 percent of the 430 ft/sec free-stream flow. This velocity lag which is a function of particle size is paramount in the determination of particle forces. Since most particles in naturally occurring sand/dust storms are non-spherical, it is important to determine the effects of particle irregularity on the momentum transfer.
2. Investigate possible electrostatic effects involved in a saltation process in a simulated Martian sand/dust storm activity.

APPENDIX A

DERIVATION OF EQUATIONS

A direct application of Newton's second law of motion, commonly referred to as the force-mass-acceleration method, will be utilized in analyzing the body forces acting upon a particle mass. Newton's second law states that "the rate of change of particle momentum is equal to the net force acting on a particle and is in the direction of the net applied force." Newton's law, as stated mathematically in rectangular coordinates is

$$F_x = ma_x \tag{1a}$$

$$F_y = ma_y \tag{1b}$$

Other than body forces, such as weight, a particle in a viscous fluid encounters predominately pressure and viscous forces. In this report, the net upward forces are termed "lift", L, and the net horizontal forces in the direction of motion are termed "drag", D.

Since the horizontal displacement of a particle entrained in a gas flow results from the aerodynamic resistance of the particle, Equation (1a) may be written in terms of the defined forces as

$$D = ma_x \tag{2}$$

and, similarly, Equation (1b) may be expressed as

$$L = m(a_y + g) \tag{3}$$

Combining Equations (2) and (3) results in the lift to drag ratio of a particle as a function of the components of acceleration

$$L/D = \frac{a_y + g}{a_x} \tag{4}$$

Dimensional analysis of some of the parameters governing particle drag leads to a grouping known as the drag coefficient (C_D).

$$C_D = \frac{D}{1/2\ \rho_\infty U_R^2 A} \tag{5}$$

Further analysis indicates that C_D is dependent upon the Reynolds number ($Re_d = \frac{\rho_\infty d U_R}{\mu}$), and Mach number ($M = \frac{U_R}{c}$).

For computational ease, Equations (2) and (5) can be combined, thus

$$C_D = \frac{4\ \rho_p\ d\ a_x}{3\ \rho_\infty\ U_R^2} \tag{6}$$

for spherical particles of uniform density. To insure proper understanding of the flow relative to the particles, the particle flow regime may be determined by the value $M/Re_d^{0.5}$. The limits of the various regimes are as follows:[32]

Range	Regime
$\frac{M}{Re_d} > 3$	Free Molecular Flow
$10^{-2} < \frac{M}{Re_d^{0.5}} \leq 10^{-1}$	Slip Flow Regime
$10^{-1} < \frac{M}{Re_d^{0.5}} \leq 3\ Re_d^{0.5}$	Transition Regime
$\frac{M}{Re_d^{0.5}} \leq 10^{-2}$	Continuum Regime

APPENDIX B

ERROR ANALYSIS

In order to assess the validity of the experimental results, an error analysis[33] was performed on L/D and on C_D in Appendix A. The probable error in L/D can be written

$$P(L/D) = \left| \left(\frac{\partial (L/D)}{\partial g} \right)^2 \delta g^2 + \left(\frac{\partial (L/D)}{\partial a_y} \right)^2 \delta a_y^2 + \left(\frac{\partial (L/D)}{\partial a_x} \right)^2 \delta a_x^2 \right|^{1/2} \qquad (1)$$

where

$$\frac{\partial (L/D)}{\partial g} = \frac{1}{a_x} = \frac{L/D}{g + a_y}$$

$$\frac{\partial (L/D)}{\partial a_y} = \frac{1}{a_x} = \frac{L/D}{g + a_y}$$

$$\frac{\partial (L/D)}{\partial a_x} = -\frac{g + a_y}{a_x^2} = -\frac{L/D}{a_x}$$

Substituting the above into Equation (1), we have

$$P(L/D) = \left| \left(\frac{L/D}{g + a_y} \right)^2 \delta g^2 + \left(\frac{L/D}{g + a_y} \right)^2 \delta a_y^2 + \left(\frac{L/D}{a_x} \right)^2 \delta a_x^2 \right|^{1/2}$$

or

$$P(L/D) = L/D \left| \left(\frac{\delta g}{g + a_y} \right)^2 + \left(\frac{\delta a_y}{g + a_y} \right)^2 + \left(\frac{\delta a_x}{a_x} \right)^2 \right|^{1/2}$$

Since g is constant, $\delta g = 0$ and we have for the probable percent error in L/D

$$\frac{P(L/D)}{L/D} = \left| \left(\frac{\delta a_y}{g + a_y} \right)^2 + \left(\frac{\delta a_x}{a_x} \right)^2 \right|^{1/2} \qquad (2)$$

Similarly, the probable percent error in C_D is

$$\frac{P(C_D)}{C_D} = \left\{ \left(\frac{\delta\rho_p}{\rho_p}\right)^2 + \left(\frac{\delta a_x}{a_x}\right)^2 + \left(\frac{\delta d}{d}\right)^2 + \left(\frac{\delta\rho_\infty}{\rho_\infty}\right) + 4\left(\frac{\delta U_\infty}{U_R}\right)^2 + 4\left(\frac{\delta U_p}{U_R}\right)^2 \right\}^{1/2} \qquad (3)$$

APPENDIX C

REFERENCES

1. Bagnold, R. A., The Physics of Blown Sand and Desert Dunes, Methuen Ltd., 1941.

2 Owen, P. R., "Saltation of Uniform Grains in Air," Journal of Fluid Mechanics, Vol. 20, Part 2, pp. 225 - 242, 1964.

3. Wilst, G. R., and Nickola, P. W., "On the Wind Erosion of Small Particles," Bulletin American Meteorological Society, Vol. 40, No. 2, 1959.

4. Sutherland, A. J., "Entrainment of Fine Sediments by Turbulent Flows," PhD Thesis, California Institute of Technology, Pasadena, California, 1966.

5. Kadib, A. A., "Function for Sand Movement by Wind," Hydraulic Engineering Laboratory Report HEL 2-12, University of California, 1965.

6. Ryan, J. A., "Notes on the Martian Yellow Clouds," Journal of Geophysical Research, Vol. 69, No. 18, pp. 3759 - 3770, 1964.

7. Michaux, C. M., Handbook of the Physical Properties of the Planet Mars, NASA SP-3030, U. S. Government Printing Office, 1967.

8. Hertzler, R. G., "Particle Behavior in a Simulated Martian Environment," McDonnell Aircraft Co., Report E418, 1966.

9. Hertzler, R. G., "Behavior and Characteristics of Simulated Martian Sand and Dust Storms," McDonnell Aircraft Co., Report E720, 1966.

10. Jeffreys, H. J., "On The Transport of Sediments By Streams," Proceedings of the Cambridge Philosophical Society, Vol. 25, pp. 272 - 6, 1929.

11. Chepil, W. S., "Equilibrium of Soil Grains at the Threshold of Movement by Wind," Soil Science Society of American Proceedings, Vol. 23, No. 6, pp. 422 - 428, 1959.

12. Torobin, L. B. and Gauvin, W. H., "Introductory Concepts and Idealized Sphere Motion in Viscous Regime," The Canadian Journal of Chemical Engineering, 37:129, 1959.

13. Torobin, L. B. and Gauvin, W. H., "The Sphere Wake in Steady Laminar Fluids," The Canadian Journal of Chemical Engineering, 37:167, 1959.

14. Torobin, L. B. and Gauvin, W. H., "Accelerated Motion of a Particle in a Fluid," The Canadian Journal of Chemical Engineering, 37:224, 1959.

15. Torobin, L. B. and Gauvin, W. H., "The Effects of Particle Rotation, Roughness, and Shape," The Canadian Journal of Chemical Engineering 38:142, 1960.

16. Torobin, L. B. and Gauvin, W. H., "The Effects of Fluid Turbulence on the Particle Drag Coefficient," The Canadian Journal of Chemical Engineering, 38:189, 1960.

17. Schiller, L. and Nauman, A., Z. Ver. deut. Ing., 77:318, 1933.

18. Ingebo, R. D., "Drag Coefficients for Droplets and Solid Spheres in Clouds Accelerating in Airstreams," NASA 3762, 1956.

19. Langmuir, I. and Blodgett, K., "A Mathematical Investigation of Water Droplet Trajectories," Army Air Forces Technical Report No. 5418, 1946.

20. Millikan, R. A., "The General Law of Fall of a Small Spherical Body Through a Gas, and its Bearing Upon the Nature of Molecular Reflection from Surfaces," Physical Review, Vol. 22, pp. 1 - 23, 1923.

21. Carlson, D. J. and Hoglund, R. F., "Particle Drag and Heat Transfer in Rocket Nozzles," AIAA Journal, Vol. 2, No. 11, 1964.

22. Rudinger, G., "Experiments on Shock Relaxation in Particle Suspensions in a Gas and Preliminary Determination of Particle Drag Coefficients," Project Squid Technical Report CAL-90-P, 1963.

23. Selberg, B. P., "Shock Tube Determination of the Drag Coefficient of Small Spherical Particles," NASA CR-418, 1966.

24. Gilbert, M., Davis, D., and Altman, D., "Velocity Lag of Particles in Linearly Accelerated Combustion Gases," Jet Propulsion, Vol. 25, No. 26, 1955.

25. Luthander, S. and Rydberg, A., Physikalische Zeitschrift, (Leipzig), 36:552, 1935.

26. Nisi, H. and Porter, A., Philosophical Magazine, 46:754, 1923.

27. Lunnon, R. G., "Fluid Resistance to Moving Spheres," Proceedings of the Royal Society, Series A, Vol. 110, 1926.

28. Schetzer, J. and Kuethe, A., Foundations of Aerodynamics, John Wiley and Sons, Second Edition, 1967.

29. Bugliarello, G., "La Resistenza al Moto Accelerto di Sfere in Acqua," Richerca Scientifica, 26:437, 1956.

30. Maccoll, J. W., Journal of the Royal Aeronautical Society, 32:777, 1928.

31. Taneda, S., Reports of Research Institute for Applied Mechanics, 5:123, 1957.

32. Emmons, H. W., "Fundamentals of Gas Dynamics," High Speed Aerodynamics and Jet Propulsion, Vol. 3, Princeton University Press, 1958.

33. Beers, Y., Introduction to the Theory of Error, Addison-Wesley Publishing Co., 1957.

ABSTRACT

An experimental investigation has been conducted to study the behavior of sand particles under simulated Martian wind conditions. Drag coefficients and lift to drag ratios were determined for particles in the 297 to 420-micron size range in air at a pressure of approximately 9 millibars, and at wind velocities up to 220 ft/second. Techniques were developed to inject particles into the wind stream under controlled conditions, to photographically record the particles trajectories, and to compute the particle accelerations and force coefficients. A particle flux detector was also evaluated but would require further development to be completely satisfactory.

An analysis of the tracks of freely falling particles in the wind tunnel revealed: (1) drag coefficients less than predicted by Stokes law (Reynold Number Range 4 to 10), (2) particle velocity/gas velocity ratios ranging from 8 to 16 (sand particles between 297 and 420 microns in size), (3) lift/drag ratios ranging from +1 to -1 with no apparent pattern, (4) the saltation process seemed to be a necessary forerunner of the entrainment process.